HHS Public Access

Author manuscript

Biomaterials. Author manuscript; available in PMC 2024 July 09.

Published in final edited form as:

Biomaterials. 2023 October ; 301: 122289. doi:10.1016/j.biomaterials.2023.122289.

Injectable Hydrogel for Sustained Delivery of Progranulin Derivative Atsttrin in Treating Diabetic Fracture Healing

Lida Moradi[a,b], **Lukasz Witek**[c,d], **Vasudev Vivekanand Nayak**[c], **Angel Cabrera Pereira**[c], **Ellen Kim**[a], **Julia Good**[a], **Chuanju Liu**[a,b,e,*]

[a]Department of Orthopaedics Surgery, New York University Grossman School of Medicine, New York, NY, 10003, USA

[b]Department of Orthopaedics & Rehabilitation, Yale University School of Medicine, New Haven, CT, 06510, USA

[c]Biomaterials Division – Department of Molecular Pathobiology, New York University College of Dentistry, New York, NY 10010, USA

[d]Department of Biomedical Engineering, New York University Tandon School of Engineering, Brooklyn, NY 11201, USA

[e]Department of Cell Biology, New York University Grossman School of Medicine, New York, NY 10016, USA.

Abstract

Hydrogels with long-term storage stability, controllable sustained-release properties, and biocompatibility have been garnering attention as carriers for drug/growth factor delivery in tissue engineering applications. Chitosan (CS)/Graphene Oxide (GO)/Hydroxyethyl cellulose (HEC)/β-glycerol phosphate (β-GP) hydrogel is capable of forming a 3D gel network at physiological temperature (37°C), rendering it an excellent candidate for use as an injectable biomaterial. This work focused on an injectable thermo-responsive CS/GO/HEC/β-GP hydrogel, which was designed to deliver Atsttrin, an engineered derivative of a known chondrogenic and anti-inflammatory growth factor-like molecule progranulin. The combination of the CS/GO/HEC/β-GP hydrogel and Atsttrin provides a unique biochemical and biomechanical environment to enhance fracture healing. CS/GO/HEC/β-GP hydrogels with increased amounts of GO exhibited rapid sol-gel transition, higher viscosity, and sustained release of Atsttrin. In addition, these hydrogels exhibited a porous interconnected structure. The combination of Atsttrin and hydrogel successfully promoted chondrogenesis and osteogenesis of bone marrow mesenchymal stem cells (bmMSCs) *in vitro*. Furthermore, the work also presented *in vivo* evidence that injection of Atsttrin-loaded CS/GO/HEC/β-GP hydrogel stimulated diabetic fracture healing by simultaneously inhibiting inflammatory and stimulating cartilage regeneration and endochondral bone formation signaling

*Correspondence: chuan-ju.liu@yale.edu or chuanju.liu@nyulangone.org.

Author Contributions: L. Moradi performed *in vitro* and *in vivo* experiments, analyzed data and wrote the paper. L. Witek and V. Vivekanand designed the experiments for hydrogel characterization and edited the manuscript. A. C. Pereira performed the nanoindentation test, E. Kim and J. Good performed the MicroCt experiment and edited the paper, and C. J. Liu conceived and supervised study, analyzed data, and edited the manuscript.

Competing interests

The authors declare no competing interests.

pathways. Collectively, the developed injectable thermo-responsive CS/GO/HEC/βG-P hydrogel yielded to be minimally invasive, as well as capable of prolonged and sustained delivery of Atsttrin, for therapeutic application in impaired fracture healing, particularly diabetic fracture healing.

Graphical abstract:

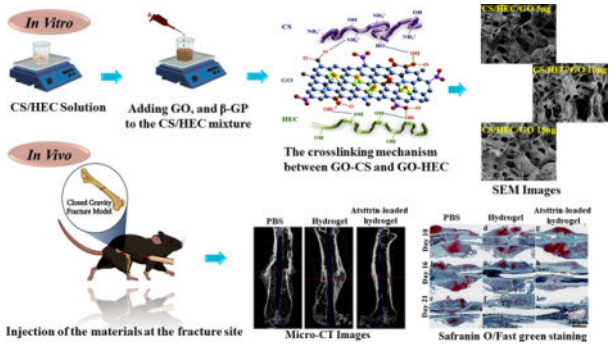

Preparation of hydrogel solutions, the schematic crosslinking mechanism between the CS and HEC with GO, and a single dose injection of the materials at the fracture site immediately after inducing femur fracture in mouse closed gravity-induced fracture model.

Keywords

Injectable hydrogel; Progranulin; Atsttrin; diabetes; fracture healing; impaired fracture healing

1. Introduction

Bone defects resulting from trauma, disease, or age-related factors have a significant impact on patients, affecting their functional abilities and psychological well-being [1]. Diabetes mellitus (DM), a prevalent inflammatory autoimmune condition associated with high blood sugar levels and chronic inflammation, further exacerbates the risk of fractures and impairs the quality of bone fracture healing. This is primarily attributed to the promotion of osteoclastogenesis, the excessive loss of cartilage, and the increased susceptibility of metabolically compromised individuals to bone regeneration challenges [1–3]. Under diabetic conditions, the fluctuation of glucose levels exerts a particularly detrimental effect on tissue regeneration. This can give rise to metabolic disorders and impaired mitochondrial function, leading to an increased generation of reactive oxygen species (ROS) which exacerbates inflammation and contributes to the degradation of host tissues, creating a pro-inflammatory microenvironment at the bone fracture site [4]. Consequently, the process of fracture healing is significantly compromised, posing a significant challenge for bone regeneration in individuals with diabetes [5, 6]. This is further evidenced by the remarkably elevated level of inflammatory cytokines, such as tumor necrosis factor-α (TNF-α), interleukin-1β (IL-1β), and interleukin-6 (IL-6) [3, 5].

Considering the significant role of elevated inflammatory cytokines in the process of fracture healing, the precise coordination and harmonization of diverse biological events

are of utmost importance. Nonetheless, achieving this level of coordination poses a persistent challenge in the field of bone tissue regeneration. One area of interest lies in the development of treatment strategies that can effectively target and regulate the impact of the inflammatory cytokines. This holds promise as a potential approach to improve bone healing, especially in the context of diabetic conditions by restraining the power of inflammatory cytokines. Such strategies could represent a significant advancement in enhancing the regenerative capacity of bone tissue. To attain successful healing, it is essential to consider the intricate and constantly evolving pathological microenvironment of DM and its impact on the regenerative processes of the host. In the field of tissue regeneration, significant strides have been made in understanding the critical role of the microenvironment. This newfound knowledge has opened doors to innovative approaches that employ materials to manipulate cellular behaviors by remodeling the microenvironment [7]. Of particular interest are hydrogels, which have emerged as promising candidates for such strategies. Hydrogels offer a unique platform due to their ability to mimic the natural extracellular matrix (ECM) and provide a conducive environment for tissue regeneration [8, 9]. By leveraging the properties of hydrogels, researchers have been able to precisely control cell responses, guide tissue growth, and enhance therapeutic outcomes. One particularly exciting application is the utilization of hydrogels for the controlled release of drugs, allowing for targeted and sustained delivery to the site of interest. These advancements in hydrogel-based systems hold immense potential for advancing tissue engineering and regenerative medicine, offering new avenues to optimize the microenvironment and enhance tissue regeneration processes.

Hydrogels, with their distinctive three dimensional (3D) network structure composed of hydrophilic polymers, possess exceptional hydrophilicity and biocompatibility [10]. The structural elasticity of hydrogels renders them highly advantageous for tissue regeneration, making them prominent in biomedical application, drug delivery, tissue regeneration, and antibacterial therapy [11]. 3D porous hydrogels have emerged as a promising strategy to enhance bone regeneration by virtue of their robust hydrophilic networks of interlinked polymeric units, enabling them to absorb significant amounts of water without disintegration [12–18]. Injectable or in situ forming hydrogels are particularly explored in orthopedic applications as minimally invasive alternatives for addressing diverse bone defects, eliminating the need for revision surgeries. The hydrophilic nature of these hydrogels imparts them with elastic properties, affording stress resistance and fluid retention capabilities [14, 19]. Both natural and synthetic polymer-based hydrogels are under investigation for their potential to support bone tissue regeneration, with natural polymers being favored due to their resemblance to native ECM components and their adaptability for achieving specific biological responses [20]. Natural polymers like chitosan (CS) exhibit desirable attributes, including safety, biocompatibility, promotion of mineralized bone matrix formation, and osteoconductive properties [15, 21–25]. In recent years, graphene oxide (GO) has attracted attention for its unique physicochemical properties and biocompatibility, showing potential to enhance osteogenic differentiation and bone formation. GO demonstrates interactions with proteins through hydrophobic and electrostatic forces, which hold the potential to enhance the osteogenic differentiation of progenitor cells and promote bone formation [26, 27]. Hydroxyethyl cellulose (HEC)-

derived scaffolds also emulate the native ECM microenvironment, promoting cellular adhesion, growth, and calcium deposition. They serve as suitable substrates for cellular attachment and proliferation, with controlled degradation, and enhanced swelling. These findings highlight the immense potential of HEC-based hydrogel in bone regeneration [28, 29].

β-glycerophosphate (β-GP) possesses the capacity to induce diffuse calcification via an Alkaline phosphatase (ALP)-dependent mechanism. This *in vitro* calcification system, which is facilitated by β-GP, serves as a valuable tool for examining the molecular and cellular mechanisms that underlie vascular calcification [30, 31].

Progranulin (PGRN) and its derivative Atsttrin are recognized for their ability to bind to and modulate TNF-α receptors [32–37]. Both PGRN and Atsttrin effectively stimulated the proliferation and chondrogenic differentiation of bone marrow mesenchymal stem cells (bmMSCs) *in vitro* and protected against osteoarthritis (OA) phenotype *in vivo* via stimulation of TNFR2-dependent chondrocyte anabolism, and inhibition of TNFα/TNFR1-induced inflammation and catabolism [38–43]. Additionally, recombinant PGRN administration promoted callus formation and endochondral ossification during bone fracture healing under both physiological and diabetic conditions [3, 43–46]. Further, administration of a single-dose intra-articular injection of Atsttrin-loaded peptide-based hydrogel successfully protected both articular cartilage and subchondral bone quality in rabbit post-traumatic OA (PTOA) models [47]. These findings provide new insights concerning the role of exogenous engineered Atsttrin as a promising alternative therapeutic agent for the treatment of TNF-α-related inflammatory diseases such as delayed fracture healing in diabetes patients. In order to induce the proper callus formation and endochondral bone regeneration, it is important to provide a unique biomechanical and biochemical environment to enhance the efficacy of Atsttrin at the fracture site.

The objective of this study was to design and prepare a novel thermoresponsive injectable hydrogel composed of CS, GO, HEC, and β-GP, as a carrier for PGRN, with a specific focus on its derivative Atsttrin. The hydrogel is intended to provide controlled and sustained release of Atsttrin at the fracture site over an extended period. Our group previously utilized thermo-responsive injectable CS/HEC/β-GP hydrogels for the controlled delivery of nerve growth factor and cell-based therapeutics for spinal cord regeneration [48]. To the best of our knowledge, there is no effort in using thermosensitive hydrogels composed of CS/GO/HEC/β-GP as carriers for Atsttrin-concentrated for bone fracture healing in subjects diagnosed with type 1 DM (T1DM). In this study, four different types of hydrogels were fabricated in which, CS and HEC were crosslinked by GO, and β-GP was used as a gelation agent. Hydrogels were characterized using various assays including FTIR, swelling and degradation rate, cytotoxicity, *in vitro* release of Atsttrin, SEM, as well as chondrogenic and osteogenic capability of bmMSCs. In addition, the efficacy of hydrogels loaded with Atsttrin and underlying molecular events were determined using a closed gravity-induced femur fracture mouse model and RNA-Seq analysis, respectively.

2. Materials & Methods

All used chemicals were obtained from Sigma-Aldrich, USA unless otherwise noted. Primary Anti-Atsttrin antibody was supplied by Lampire Biological Laboratories (Pipersville, PA, USA). Biotinylated goat Anti-Rabbit IgG (H + L), was purchased from Vector Laboratories. All cellular and animal protocols including cell isolation, maintenance, handling, and surgical procedures were reviewed and approved by the Institutional Animal Care and Use Committee (IACUC), New York University (NYU), NY, USA.

2.1. Preparation of Thermoresponsive Injectable CS/GO/HEC/β-GP Hydrogels

CS/GO/HEC/β-GP hydrogels were prepared using the following steps as previously established with some modifications [48]. Firstly, CS solution (1.5% w/v), was prepared by dissolving 150 mg of CS powder (medium molecular weight, USA) in 15 mL acetic acid (0.1 % v/v). HEC solution (2.5 % w/v) was prepared by dissolving 250 mg HEC (average MW~90,000) in 10 mL distilled water. GO sheets dispersed in H_2O (4 mg/mL) were treated by ultrasonication for 2 hours before use; and 750 mg of β-GP (MW = 216.04 g/mol) was dissolved in 1.5 mL deionized H_2O. The CS and GO solutions were subjected individually to gamma radiation (1000G). On the other hand, the β-GP and HEC solutions underwent filter sterilization to ensure their sterility for *in vitro* cell-based experiments as well as for *in vivo* study. Secondly, equal volumes (1:1) of CS and HEC solutions were mixed, after which a calculated amount of GO dispersion in H_2O was added dropwise to the CS and HEC mixture under continuous stirring for 2–3 hours at 4 °C until achieving complete translucent mixtures of 5 μg/mL, 10 μg/mL and 15 μg/mL GO solutions. Finally, 125 μL β-GP solution as the gelation agent was added to the CS/HEC, CS/HEC/GO 5 μg, CS/HEC/GO 10 μg, and CS/HEC/GO 15 μg mixed solutions under continuous stirring and under aseptic condition. The CS/HEC/β-GP solution without GO was considered to be the control group. According to the amount of GO in each solution, the samples were grouped as CS/HEC/β-GP (nominated as CS/HEC, the control group), CS/GO 5 μg/HEC/β-GP (nominated as CS/HEC/GO 5 μg), CS/GO 10 μg/HEC/β-GP (nominated as CS/HEC/GO 10 μg), and CS/GO 15 μg/HEC/β-GP (nominated as CS/HEC/GO 15 μg) hydrogels.

2.2. Hydrogels Characterization

2.2.1. Fourier Transforms Infrared (FTIR) Spectroscopy—The FTIR spectra were carried out using a CRUSHIR digital hydraulic press spectrophotometer, employing KBr pellets as the sample preparation method. The spectra encompassing a range from 4000 to 500 cm^{-1} were collected and analyzed for the various samples, including pure CS, HEC, β-GP and, GO powders. Additionally, FTIR spectra were obtained for all control and experimental hydrogels.

2.2.2. Rheological Measurement—The test tube inverting method was employed to measure the gelation time of all hydrogel groups in a water bath at a constant temperature of 37 °C. A volume of 5 mL of each specimen was added into test tubes at room temperature, then incubated in the water bath. The fluidity of the samples was observed by tilting the tube. The time at which flow stopped was taken as the gelation time and the values were recorded.

To evaluate the rheological properties of the hydrogels in the gelling process, rheology test was assessed using a DHR-3 rheometer (TA instruments, USA). The oscillation temperature ramp was conducted over a temperature range of 4–45 °C with the ramp rate of 2 °C/min, soak time 30 seconds, soak time after ramp 30 seconds, strain 1% and frequency of 1 Hz. The 1 mL of the solutions of all hydrogels were steadily deposited onto the bottom plate of the rheometer with a diameter of 20 mm and a gap of 1000 μm. The gelation temperature was recorded as the crossover point of the dynamic rheological properties including storage (elastic) (G') modulus and loss (viscous) (G'') modulus. The experiments were carried out with 3 replicates.

2.2.3. Swelling Test—For water uptake measurements, CS/HEC and CS/HEC/GO hydrogels were prepared and weighed and recorded as W0 (initial weight) before being soaked in 1X phosphate buffered saline (PBS) solution at room temperature. At the end of each time point (1, 2, 4, 8,12, 24, 48, and 72 hours), the specimens were removed from PBS, wiped off the excess water on the surface with filter paper, and weighed to determine the wet weight which was noted as Wt (final weight) as a function of the soaking time. The swelling ratio was defined according to the following equation:

$$\text{Swelling rate}(\%) = \left(\frac{Wt - W0}{W0}\right) \times 100$$

The experiments were carried out with 3 replicates.

2.2.4. Degradation Test—To evaluate the hydrolytic degradation behavior of the hydrogels, an *in vitro* degradation study was conducted in a PBS solution. The hydrogels were prepared and immersed in PBS, followed by incubation at 37 °C for 8 weeks. Fresh PBS was exchanged weekly to maintain the degradation environment. At predetermined time intervals (1, 2, 3, 4, 5, 6, 7, and 8 weeks), the hydrogels were removed from the PBS, dried at 37 °C in an oven for 24 hours, and weighed. The degradation rate was calculated using the following equation,

$$\text{Degradation rate}(\%) = (\text{Wt}_{\text{initial}} - \text{Wt}_{\text{dry}})/\text{Wt}_{\text{initial}} \times 100$$

The experiments were carried out with 3 replicates.

2.2.5. In Vitro Atsttrin Release Study using Indirect ELISA—The amount of Atsttrin released from all hydrogel groups over 8 weeks was assessed using indirect ELISA. Atsttrin with a final concentration of 1 μg/μL was added and mixed with CS/HEC and CS/HEC/GO solutions, and then incubated at 37 °C for 30 minutes to form gels. At predetermined time points (days 1, 2, 3, 4, 5, 6, 7, and weeks, 2, 3, 4, 5, 6, 7, and 8), all PBS was collected and replaced with fresh PBS. Subsequently, 100 μL of collected PBS was added to the 96-well culture plate and maintained at 4° C overnight. Then, the PBS solution was removed, and 200 μL of 5% non-fat dry milk in PBS (1706404 & BIO-RAD, USA) was added to each well as a blocking agent and kept at room temperature for 2 hours. Next, after washing the plate 3 times with PBS, 100 μL of primary anti-Atsttrin antibody (diluted 1:1000) within the blocking agent was added to each well and incubated overnight at 4 °C.

The following day, the plate was rinsed 3 times with PBS, and then, 100 μL of secondary goat Anti-Rabbit Antibody diluted in blocking agent (1:5000), added and incubated for 1–2 hours at room temperature. Then, the plate was rinsed 3 times with PBS, and 100 μL of the mixture of copper sulfate solution and the bicinchoninic acid solution was added to each well and incubated for 10 minutes at room temperature. Lastly, 100 μL of 2 M sulfuric acid (H_2SO_4) was added and read the optical density (OD) at 450 nm using a spectrophotometer (Stat Fax, USA). The experiments were carried out with 3 replicates.

2.2.6. Cell Viability and Cell Proliferation—All experiments (harvesting of cells and surgical procedure) were approved by the Institutional Animal Care and Use Committee (IACUC, IA15–01372), New York University in this study. Six-eight-week-old C57BL/6 mice (n=5) were sacrificed by cervical dislocation. To isolate bone marrow-derived mesenchymal stem cells (bmMSCs), femur and tibia were harvested under aseptic conditions and washed in PBS containing antibiotic/antimycotic solution (1 %, Invitrogen, USA) and put in 1.5 mL sterile microtube and centrifuged for 5 minutes, 1300 rpm. The viability of isolated cells was measured by trypan blue staining using a hemocytometer. Isolated cells were suspended in Dulbecco's modified Eagle's medium (DMEM) (Gibco, USA) supplemented with 10% fetal bovine serum (FBS; Gibco, USA), and antibiotic/antimycotic, plated in six well cell culture plate and incubated at 37 °C, 5% CO_2. Media changed twice a week.

MTT assay (3-[4, 5-dimethylthiazol-2-yl]-2,5-diphenyltetrazolium bromide) was employed as previously described to assess the cytotoxicity effect of the different concentration of GO ranging from 10 μg/mL to 60 μg/mL as well as the cytotoxicity effect of prepared hydrogels on bmMSCs [49]. To evaluate the cytotoxicity of GO, the mice isolated bmMSCs at passage three were used and seeded at a density of 2×10^4 cells/well in a 96-well cell culture plate and incubated at 37 °C with 5% CO_2 overnight to allow cell attachment. Cells cultured without the GO served as the control group. The following day varying concentrations of GO at 10, 20, 30, 40, 50, and 60 μg/mL were added into the DMEM media supplemented with 10% FBS and incubated at 37 °C with 5% CO_2. After 24 hours incubation, media in each well was discarded, cells washed with 1X PBS, then 100 μL of MTT solution (5 mg/mL in 1X PBS) added to each well and incubated for 4 hours at 37 °C, 5% CO_2. Finally, the MTT solution was discarded, and the formed formazan crystals were dissolved in 100 μL of dimethyl sulfoxide (DMSO) for 20 minutes at room temperature. The purple solutions' OD was measured in an ELISA plate reader (Stat Fax, USA) at 570 nm. The relative viability (%) normalized by control according to the following equation:

$$\%\ Viability = \frac{Average\ OD\ of\ samples}{Average\ OD\ of\ control\ group} \times 100$$

The experiments were carried out with 5 biological replicates. The measurements were reported as means ± standard deviations (SD).

To evaluate the cytotoxicity of the prepared hydrogels, the mice isolated bmMSCs at passage three were seeded at a density of 2×10^4 cells/well in a 96-well cell culture plate and incubated at 37 °C with 5% CO_2 overnight to allow cell attachment. The following

day prepared hydrogels with and without GO were floated into each well of the cell culture plate. Cells cultured with the hydrogel without GO served as the control group. At each designated incubation period (1, 3, and 7 days) the floated hydrogels were first removed from the wells, then cells washed with 1X PBS and finally MTT assay performed as described above. The experiments were carried out with 5 biological replicates. The measurements were reported as means ± standard deviations (SD).

2.2.7. Scanning Electron Microscopy (SEM)—The prepared hydrogels were fixed with 4 % Paraformaldehyde (PFA) for 45 minutes to preserve their structure. Following fixation, hydrogels were washed with distilled H_2O and dehydrated using a series of ethanol solutions (50%, 70%, 95%, and twice with 100%) with each step lasting 5 minutes. Subsequently, the dehydrated hydrogels were subjected to overnight freeze-drying to remove any residual moisture. The freeze-dried hydrogels were then gold coated and imaged using a VEGA TESCAN Inc. USA SEM instrument. Three images were captured for each group. The obtained SEM images were further analyzed using the ImageJ software bundled with Zulu OpenJDK 13.0.6 (version 1.53, USA) to measure the pore size of the hydrogels.

2.2.8. Thermogravimetric (TGA) Analysis—Thermal stability of the CS/HEC/GO 10μg hydrogel and CS/HEC/GO 10μg hydrogel containing 1000 ng/mL Atsttrin was measured by TGA analysis (SDTQ600 TG analyzer, TA Instruments, New Castel, Delaware, USA). Approximately 20 mg of fresh hydrogels were weighed into the platinum pan. After inserting the pan into the TG analyzer, the sample was heated from 25 to 150 °C with at a heating rate of 5 °C min^{-1} under N_2/O_2 atmosphere with a flow rate of 25 ml min^{-1}. The data were analyzed using TA Universal Analysis software, USA.

2.2.9. Anti-inflammatory effect of Atsttrin—Murine macrophage-like cells, RAW264.7 were seeded in 6-well plates at a density of 5×10^3 cells/cm^2. The plates were then incubated at 37 °C with 5% CO_2 overnight to allow for cell attachment. The study aimed to investigate the expression levels of inflammatory cytokines, specifically interleukin-6 (IL-6) and inducible nitric oxide synthase (iNOS), in RAW264.7 cells after 24 hours of treatment with TNF-α and Atsttrin. The following experimental groups were established for this purpose: The RAW264.7 cells cultured in DMEM/10%FBS only (control group), the RAW264.7 cell cultured in DMEM/10%FBS supplemented with 10 ng/mL TNF-α in media (TNF-α group), and the RAW264.7 cell cultured in DMEM/10%FBS supplemented with 10 ng/mL TNF-α in media and hydrogel loaded with 1000 ng/mL Atsttrin (Hydrogel group). Quantitative reverse transcription polymerase chain reaction (qRT-PCR) was employed to measure the expression levels of IL-6 and iNOS in each group. All experiments were conducted in triplicate. This experimental design allowed for the assessment of the potential anti-inflammatory effects of Atsttrin-loaded hydrogels on RAW264.7 cells stimulated with TNF-α.

2.2.10. *In Vitro* Chondrogenesis and Osteogenesis—For the induction of chondrogenesis, micromass culture was done for 10 days with mice bmMSCs. A chondrogenic differentiation medium, composed of DMEM supplemented with 10 % FBS 10^{-7} M dexamethasone, 1 % ITS and, 50 μg/mL ascorbate 2-phosphate was used. In detail,

15×10^4 bmMSCs, at passage three, in 20 μL chondrogenic media were directly seeded at the center of a 24-well cell culture plate and incubated at 37 °C with 5 % CO_2 to allow cell aggregation. After 3 hours, the chondrogenic medium was carefully added, prepared hydrogels immersed to the wells and then incubated for 10 days before the evaluation of chondrocyte differentiation in predetermined time points (3, 7, and 10 days). The micromass culture of bmMSCs was performed in the presence of the chondrogenic media (cells cultured without the hydrogel, or hydrogel loaded with Atsttrin (control group), hydrogel only + chondrogenic media (hydrogel group), and hydrogel loaded with 1000 ng/mL of Atsttrin + chondrogenic media (Atsttrin-loaded hydrogel group). The prepared hydrogels were floated into the media of each well of the hydrogel and Atsttrin-loaded hydrogel groups. At each designated incubation period, the floated hydrogels were first removed from the wells. Cells were washed with PBS and fixed with 4% PFA for 30 minutes at room temperature, rinsed twice with PBS and stained with alcian blue solution pH 2.5 (1% w/v) (alcian blue 8GX in 100 mL acetic acid 3%) for 30 minutes at room temperature and in dark to evaluate the level of glycosaminoglycans (GAGs) accumulation. The reactions were stopped by rinsing with PBS and observed under a light microscope (Nikon TS100, USA). Further evaluation was conducted for the expression of cartilage anabolic factors including aggrecan (ACAN), collagen type II alpha 1 (Col2a1), and sex-determining region Y (SRY)-box transcription factor 9 (Sox-9) by quantitative real-time polymerase chain reaction (qRT-PCR) analysis. For the mRNA extraction, 15×10^4 bmMSCs cells were used, conducting three replicates (45×10^4 cells) for each group in each timepoint.

Monolayer cell culturing was carried out for osteogenic differentiation of bmMSCs for 10 days. To confirm the osteogenic potential of bmMSCs, cells at a density of 2×10^4 cells/cm^2 were seeded in 24 well cell culture plates. The osteogenic medium was composed of DMEM/10% FBS containing 10 mM β-GP, 50 μg/ml ascorbic acid, and 100 nM dexamethasone. The osteogenic differentiation was performed in the presence of osteogenic media (cells cultured without the hydrogel, or hydrogel loaded with Atsttrin (control group), hydrogel only + osteogenic media (hydrogel group) and hydrogel loaded with 1000 ng/mL of Atsttrin + osteogenic media (Atsttrin-loaded hydrogel group). At each predetermined time point (3, 7, and 10 days), the floated hydrogels were first removed from the wells, cells washed twice with PBS, fixed with 4% PFA for 30 minutes at room temperature, then washed twice with PBS and stained with 2 % Alizarin Red S pH 4.1–4.3 (2% w/v) (Alizarin red S in 100 mL distilled water) at room temperature for calcium quantification. Following 10 minutes incubation, cells washed with PBS twice and observed under a light microscope (Nikon TS100, USA). Additionally, qRT-PCR was performed to evaluate the expression of osteogenic genes including RUNX family transcription factor-2 (RUNX-2), bone morphogenetic protein-2 (BMP-2), osteocalcin (OCL), osteonectin (OCN), alkaline phosphatase (ALP) and collagen type I (Col I) at present-day 3, 7 and 10. The medium was changed twice a week.

For mRNA isolation 24×10^4 cells were used, with three replicates for each group (72×10^4 cells) in each timepoint.

2.2.11. Alkaline Phosphatase (ALP Staining)—Monolayer cell culturing was carried out for ALP staining of mice bmMSCs for 10 days and the medium was changed

twice a week. bmMSCs at passage three were cultured in 6 well plates at a density of 5×10^3 cells/cm^2 and incubated at 37 °C with 5% CO_2 overnight to allow cell attachment. The osteogenic medium was composed of DMEM/10% FBS containing 10 mM β-GP, 50 μg/ml ascorbic acid, and 100 nM dexamethasone. The osteogenic differentiation was performed in the presence of osteogenic media (cells cultured without the hydrogel, or hydrogel loaded with Atsttrin (control group)), hydrogel only + osteogenic media (hydrogel group) and hydrogel loaded with 1000 ng/mL of Atsttrin + osteogenic media (Atsttrin-loaded hydrogel group). ALP kit (purple) (abcam, USA) was used for ALP staining. Hydrogels were floated into the media of each well of the hydrogel and Atsttrin-loaded hydrogel groups. At each designated incubation period (3, 7, and 10 days) the floated hydrogels were first removed from the wells. Cells were washed with 1X PBS and fixed with fixing solution for 2 minutes at room temperature, then washed twice with 1X PBS and stained with ALP solution for 30 minutes in the dark at room temperature. The reactions were stopped by rinsing with 1X PBS and observed under a light microscope (Nikon TS100, USA). The ImageJ bundled with Zulu OpenJDK 13.0.6 software (version 1.53, USA) was utilized to calculate the OD/unit area (IOD/area) for the ALP-stained images (three images for each group), allowing for the analysis of positive ALP expression in each field of view [50].

2.2.12. mRNA Isolation and Gene Expression Analyses—The gene expression evaluation was quantified using a One-Step instrument (ABI, USA). Prior to mRNA extraction, both floated hydrogels and media were discarded, and subsequently cells washed with 1X PBS and collected by trypsinization. Total mRNAs were isolated, using Trizol reagent (Invitrogen, USA). Subsequently, DNase-digested total RNAs were reverse transcribed to produce single-strand cDNA using the PrimeScript RT Reagent Kit (TaKaRa, USA). The qRT-PCR analysis was performed using SYBR Premix Ex Taq II (Takara, USA). GAPDH was used as an endogenous control. The specific primer sequences for amplified target genes are shown in Table 1.

2.3. *In Vivo* Study

2.3.1. Diabetes Mice Model—To induce T1 DM, first sodium citrate solution (0.1 M, pH 4.5) was prepared by dissolving 1g of sodium citrate powder in 34 mL of distilled water, adjusting the pH to 4.5 with HCl. Since Streptozocin (STZ) degrades quickly in aqueous solutions, the sodium citrate buffer should be freshly prepared and STZ utilized immediately to obtain the best experimental results.

In the next step, 1 mg of STZ (S0103, Sigma, USA), was dissolved in 150 μL of 0.1 M sodium citrate buffer to produce a final concentration of 6.66 mg/mL of STZ immediately before induction. The solution then was injected intraperitoneally into each mouse, 50 mg/kg body weight, for five consecutive days. Mice with blood sugar levels less than 250–300 mg/dL over two consecutive days were excluded from the study (Table 2) [22, 23].

2.3.2. Surgical Approach—For the *in vivo* studies, 8–10-week-old C57BL/6 mice with an average weight of 20.7 ± 1.4 grams were divided into three study groups with 6 mice per group. The mice in the experimental study groups were subjected to closed gravity femur bone fracture and immediately treated with Atsttrin-loaded hydrogel (8 μg of Atsttrin/10 μL

of hydrogel) (n=6) and hydrogel (10 μL of hydrogel) (n=6). PBS group (10 μL of sterile PBS) (n=6) was used as a control with induction of a closed gravity femur bone fracture. Before bone fracture surgery, general anesthesia was performed with isoflurane in a sedation box. During surgery, first, a 1.5 cm incision was performed through the skin and fasciae centered over the knee joint followed by displacement of the patella medially to expose the distal end of the femur bone. Then, a 0.5 mm×40 mm, 25-gauge needle was inserted at the intercondylar fossa, down the length of the medullary canal in a retrograde manner, and through the proximal end of the femur. X-ray was used to ensure the proper placement of the needle (data are not shown). A 4-in-long 36-gauge tungsten guidewire was passed through the shaft of the needle, subsequently removing the needle. Femurs were then fractured using an established fracture device. To do this, the right hind leg of the mice was placed on a metal plate, and positioned horizontally across the two supporting points, such that the proximal and distal ends of the femur rested on the supporting anvils. A weight of 391 g was dropped from a height of 34.6 cm above the impacted disc, which resulted in a transverse fracture of the femur bone. Finally, the mice were carefully removed from the device immediately after inducing the fracture. At the final step, a 0.5 mm×40 mm, 25-gauge needle was inserted over the guidewire to fix the fracture site in the femur. The hydrogel with or without Atsttrin was injected into the fracture site of all femurs in two experimental groups. All mice in the PBS control group were subjected to the same procedure. The fascia was closed using a simple continuous running suture with an absorbable 6–0 vicryl, and the skin was sutured in a single-knot technique using non-absorbable 6–0 Nylon. The mice were returned to their cages and provided free access to normal water and food. They were free to move into their home cages [51].

2.3.3. Histological Staining—The six femurs for each group were harvested, fixed in 4 % PFA for 48 hours with gentle agitation at 4 °C, and washed three times, each 10 minutes with PBS to remove PFA. All samples were decalcified in 10 % EDTA pH7 for 21 days with gentle agitation at 4 °C. In the next step, samples were washed three times with 1X PBS, tissue processing performed using alcohol and xylene, embedded in paraffin, and cut into 5 μm thickness. Safranin-O/Fast Green and, Pentachrome staining was performed to visualize the cartilage and new bone tissues in the fractured femur.

2.3.4. Micro-CT Analysis—The three samples of the fractured femurs of all groups were scanned using a Scanco μCT40 cone-beam scanner (SCANCO Medical, Switzerland) set to 55 kV and 145 μAmp (Brucker micro-CT, Belgium) at the endpoint 21 days after fracture. The femurs were scanned at 10.5 μm resolution, with an isotropic pixel size of 18 μm and energy settings of 100 kV (voltage), 400 ms (exposure time), and 100 μA (current) through a 1.0-mm aluminum filter. Image reconstruction, including ring artifact reduction (20/20), beam hardening correction (30 %), and smoothing (1/10) was performed using the SkyScan NRecon software (v. 1.6.9.8, Brucker microCT, Belgium). The scanned images from each group were evaluated at the same thresholds to allow for the 3D structural reconstruction of each specimen.

2.3.5. Nanoindentation Tests—Nanoindentation tests were performed at 21 days post-surgery with three samples for each group). For each specimen three indentations per

region in the trabecular bone region, and six indentations per region in the cortical bone region were performed for a total of six and 24 indentations, respectively. The distance was adjusted between the indentations within the same specimen (1 × 3 for trabecular bone and, 2 × 3 for the cortical bone), and the distance from the edge around 15 and 30 μm, respectively. Indentations were performed on the mouse femur with a Berkovich tip (Hysitron TI Primer nanoindenter, Bruker, USA) up to a maximum load of 6,000 μN which led to a penetration depth of ~500 nm and radius of ~3,500 nm on the specimens [22, 23]. All indentations were performed with the following parameters: loading time set to 20.0 s (loading rate equal to 300 μN/s), holding time set to 30.0 s, and unloading of 6.65 s (unloading rate equal to 902 μN/s). In total, 99 indentations were assessed (78 on the cortical bone and 21 on the trabecular bone). Each load-displacement indentation curve and image of the indentation were checked for potential contact issues. For each indentation, both the modulus (GPa) and the Hardness (GPa) were computed.

2.3.6. Bulk RNA-Seq and Gene Set Enrichment Analysis—For bulk RNA-seq analyses, three femur fracture sites for each group were harvested at predetermined time points post-fracture. Total mRNA was extracted (days 10, 16, and 21) using Trizol reagent (Invitrogen, USA). During the tissue harvesting process, a rigorous procedure was implemented to ensure the precise collection of the desired area. The meticulous removal of any remaining gel around the fracture site and the flushing of the bone marrow with PBS were carried out to eliminate potential interference from the gel composition and bone marrow. Moreover, the harvested fracture site included the callus and newly formed bone, along with approximately 1mm of bone tissue from each side. This thorough removal process aimed to minimize any influence on mRNA quantity or quality from the gel composition. The sequencing library was prepared according to the steps recommended by the Illumina TrueSeq mRNA sample preparation kit. Sequencing was conducted on Illumina HiSeq 3000. STAR software was used to map the reads to the rat genome to obtain a gene expression matrix. Genes with adjusted p-value ≤ 0.05 and log2FoldChange higher than 1.5 were considered statistically significant. Gene Ontology biological process (GOBP) enrichment analysis were performed using Gene Set Enrichment Analysis (GSEA) through GSEA software.

2.4. Statistical Analysis

Statistical analysis was carried out using Prism ver. 9.4.1 software (GraphPad, USA). Obtained data are presented as mean ± SD and were analyzed using one-way and two-way analyses of variance (ANOVA) with multiple comparisons comparing multiple groups. A p-value ≤0.05 was considered statistically significant. The Student's sample t-test was used to compare the data from the experimental group with the control group.

3. Results

3.1. Fourier Transforms Infrared (FTIR) Spectroscopy

FTIR spectra were collected for pure β-GP, CS, GO, HEC, and for CS/HEC, CS/HEC/GO 5 μg, CS/HEC/GO 10 μg, and CS/HEC/GO 15 μg hydrogels to assess the interactions among functional groups of polymers and polymers with GO. As shown in Fig.1A, in the

spectrum of β-GP, characteristic peaks at 974 cm^{-1} (P–O–C), 1072 cm^{-1} (PO43), 2866 cm^{-1}, and 2924 cm^{-1} ($–CH_2$) are presented in all hydrogels with and without GO. In the spectrum of CS, two characteristic absorbance bands centered at 1590 and 1660 cm^{-1} corresponded to amide II (the N–H bending of $–NH_2$) and amide I (C=O stretching vibration of –NHCO–), respectively. The broad peak between 3340–3440 cm^{-1} corresponded to the overlapping of the O-H stretching and N-H stretching vibration. Regarding the spectrum of GO, the characteristic bands at 1725 cm^{-1} and 1621 cm^{-1} are assigned to the carboxylic acid (C=O) group and deformations of the O-H bond in water, respectively. Regarding the FTIR spectrum of HEC, the broad band at 3411 cm^{-1}, refers to stretching vibrations of the O-H group. The bands at 2924 cm^{-1} and 1060 cm^{-1} are the bands of the C—H and C—O stretching vibration, respectively. Compared to pure CS, the peak at 1590 cm^{-1} characteristic to $-NH_2$ absorbance vibration of the secondary amide shift from 1590 cm^{-1} in the pure CS spectrum to a lower wavenumber in the region of 1564 cm^{-1} in the CS/HEC spectrum (Fig.1B), and 1570–1579 cm^{-1} in the hydrogels containing GO (Fig.1B). Moreover, the 1660 cm^{-1} band shifted to a lower wavenumber around 1628 cm^{-1} in CS/HEC and 1640^{-1} in samples containing different amount of GO. These peaks are attributed to the C=O stretching vibration of –NHCO– in the amide I group [52]. A band at 1725 cm^{-1} can be assigned to the C=O stretch of the carboxylic group in GO has disappeared in the IR spectra of cross-linked hydrogels, which confirmed the successful reaction between the functional groups of CS and HEC with the functional groups of GO [53].

3.2. Rheology Measurement

The results of gelation temperature were presented in Fig. 2 and Fig. S1. In the experimental curves in Fig. 2, both G′ and G″ exhibited a reduction, indicating the typical dynamic viscoelastic behavior of biopolymer materials (G′ < G″). As the process continued, G′ decreased and reached a plateau, while G″ continued to decrease until it intersected with G′, indicating the formation of a 3D gel network [54]. The gelation temperature was calculated at the point of intersection between G′ and G″ [54]. The gel was heated at a rate of 2°C/min, reaching a temperature of 45°C after approximately 25 minutes, and the sol-gel transition was recorded. The addition of GO to CS/HEC solutions resulted in a notable decrease in the gelation temperature. Particularly, the highest concentration of GO exhibited strong reduction and rapid gelation temperature for the CS/HEC/GO 15 μg tested solution. As the temperature increased, G″ gradually decreased and eventually crossed over G′ at a certain temperature point. Different gelation temperature values were observed among the different hydrogel formulations. The gelation temperatures for CS/HEC, CS/HEC/GO 5 μg, CS/HEC/GO 10 μg, and CS/HEC/GO 15 μg were measured as 40.75 °C, 38.7 °C, 37.06 °C, and 34.65 °C, respectively (Fig. 2). Additionally, the initial G′ values varied for the different hydrogel types, measuring 1.65 Pa, 2 Pa, 2.4 Pa, and 2.7 Pa for the CS/HEC, CS/HEC/GO 5 μg, CS/HEC/GO 10 μg, and CS/HEC/GO 15 μg hydrogels, respectively.

3.3. Swelling Test

The influence of GO content on the performance of the hydrogels was further investigated through swelling tests. The swelling rate of the hydrogels with varying GO content is depicted in Fig. 3a. All hydrogels exhibited a time-dependent increase in water uptake ratio

within the first 24 hours, after which the values reached a plateau, indicating attainment of equilibrium state [55]. In general, the initial water uptake ratios exceeded 25.33 % within one hour of immersion in PBS and continue to increase with time, reaching maximum hydration equilibrium after 24 hours. Interestingly, as the GO content increased, the swelling ratio decreased from 124.197 % for CS/HEC to 100.283 % for CS/HEC/GO 15 μg after 72 hours of incubation. This observation suggests that hydrogels with higher GO content possess a more compact structure and lower water-holding capacity. The influence of GO incorporation on the swelling behavior highlights the role of GO in promoting hydrophobicity, which leads to the observed changes in swelling characteristics.

3.4. Degradation rate

All the hydrogel formulations underwent a progressive degradation process over the course of 8 weeks, as demonstrated in Fig. 3b. Among the different hydrogels, CS/HEC/GO 15 μg and CS/HEC/GO 10 μg exhibited the most favorable degradation rate, with 34.2% and 41.43% of the material undergoing degradation, respectively during first four weeks of incubation. This indicates the relatively high stability and durability of these hydrogels compared to the other hydrogels formulations. CS/HEC/GO 5 μg showed slightly higher degradation rates, with approximately 63.62% degradation, after one month of incubation in PBS. Notably, the CS/HEC hydrogel demonstrated the highest degradation rate among all the formulations, with approximately 82.62% degradation within one month. This relatively fast degradation can be attributed to the absence of graphene oxide, which may contribute to a less stable hydrogel structure. As the incubation period extended to 7 weeks, both CS/HEC/GO 10 μg and CS/HEC/GO 15 μg hydrogels exhibited substantial weight loss, with more than 83% of their initial weight being lost. On the other hand, CS/HEC/GO 5 μg and CS/HEC experienced even greater degradation, with over 95% weight loss during the same period. These observations further emphasize the degradable nature of the hydrogel formulations and their ability to undergo substantial breakdown over time. The presence of graphene oxide in the CS/HEC/GO 10 μg and CS/HEC/GO 15 μg formulations appeared to enhance their stability, resulting in a slower degradation process compared to CS/HEC/GO 5 μg and CS/HEC.

3.5. In Vitro Atsttrin Release Study using Indirect ELISA

Indirect ELISA was performed using an anti-Atsttrin antibody to calculate the release of Atsttrin from hydrogels into PBS over 8 weeks (Fig. 3c,d). All hydrogels including control and experimental groups were loaded with Atsttrin, kept at 37 °C for 30 minutes to form a gel, and then immersed in PBS for 2 months. Fig. 3c,d and Fig. S2 show the Atsttrin release profile from the hydrogels into PBS. Initially, for the first 4–5 days, there was no difference in the amount of released Atsttrin from both CS/HEC/GO 10 μg and CS/HEC/GO 15 μg hydrogels. CS/HEC and CS/HEC/GO 5 μg hydrogels showed a burst release of Atsttrin around 50.73 % and 38.07 % during the first 1 hour of incubation. After 3 weeks of incubation, they released almost 93 % and 95.3 % of Atsttrin, respectively. Then, they started to decrease the release of loaded Atsttrin into PBS. In contrast, Atsttrin release from CS/HEC/GO 10 μg and CS/HEC/GO 15 μg slowed considerably and they released 10.1 % and 11.71 % of Atsttrin during 1 hour after incubation, respectively. After 72 hours, CS/HEC/GO 10 μg released 49.68 % and CS/HEC/GO 15 μg released 33.39 % of Atsttrin.

At 6 weeks post incubation, they released 95.47 % and 89.93 % of loaded Atsttrin into PBS, respectively, and thereafter, they reached a flat plateau.

3.6. Cell Viability and Cell Proliferation

To assess the cytotoxicity of GO, bmMSCs were subjected to the MTT assay after 24 hours of incubation with varying concentrations of GO. Notably, no significant differences in cell viability were observed between the control group and the experimental groups containing GO concentrations of 10, 20, 30, and 40 μg/mL (Fig. S3). However, higher concentrations of GO, specifically 50 and 60 μg/mL, resulted in a significant decrease in bmMSC viability, with measured viabilities of 66.94% and 54.44%, respectively. These findings indicate that GO concentrations up to 40 μg/mL did not exhibit cytotoxic effects on bmMSCs. However, concentrations of 50 and 60 μg/mL displayed a concentration-dependent reduction in cell viability, surpassing the threshold for maintaining optimal cellular health. These results highlight the need for careful consideration of GO concentration when designing GO-based hydrogels to ensure biocompatibility and avoid cytotoxicity. The observed concentration-dependent cytotoxic response of bmMSCs emphasizes the importance of optimizing GO concentrations in hydrogel formulations for effective tissue engineering applications. Based on the obtained results, 15μg/mL was chosen as a high concentration of GO to prepare the hydrogels.

We next studied the cytotoxicity effect of hydrogels with different concentrations of GO on viability and proliferation rate of bmMSCs by MTT assay during 7 days (Fig. 3e,f). Cell viability assessment indicated that all hydrogels were biocompatible with bmMSCs as cell viability values for all studied hydrogels with and without GO were higher than 85.82 % after 24 hours of incubation (Fig. 3e). At day 3, cells cultured in contact with experimental hydrogels contain GO presented statistically higher proliferation than those cultured in contact with the hydrogel without GO (Fig. 3f). The same statistical significance appeared after 7 days of incubation, where cells exposed to hydrogel containing GO showed a higher proliferation rate which can assume a positive effect of hydrogels, degraded products from hydrogels, and GO on bmMSCs proliferation. Although, hydrogel with higher concentration of GO showed slight diminish in the cell proliferation rate, however there were no significant differences between this group and other hydrogels incorporating lower concentration of GO. However, further investigation is warranted to elucidate the underlying mechanisms of GO-induced cytotoxicity and to develop strategies to mitigate any potential adverse effects while harnessing the advantageous properties of GO for regenerative medicine purposes.

3.7. Scanning Electron Microscopy (SEM)

The bulk morphology of the hydrogels was evaluated through SEM imaging (Fig. 4). Fig. 4a–h exhibit a cross-sectional view of the lyophilized porous hydrogels, revealing a rough surface area, homogenous pore distribution, and interconnected microstructure. The addition of different quantities of GO to the hydrogel system resulted in noticeable alterations in pore size and pore wall thickness in comparison to the CS/HEC control hydrogel. Specifically, the hydrogels containing GO exhibited smaller pore sizes and thicker pore walls. In contrast, the CS/HEC control hydrogel exhibited thinner pore walls and larger pore sizes. The

introduction of GO into the gelation system resulted in a gradual reduction in the percentage of pore area (Fig. 4i). For instance, the CS/HEC hydrogel had a pore area percentage of 59.82%. However, as the amount of GO increased in the hydrogel formulation, the pore area percentage decreased to 48.12% for the CS/HEC/GO 15 μg hydrogel.

Based on a comprehensive assessment of rheology, swelling tests, SEM observations, in vitro Atsttrin release, and MTT evaluations, we have identified CS/HEC/GO 10μg as the optimal hydrogel for subsequent *in vitro* and *in vivo* investigations. The MTT data showed no significant differences in cytotoxicity and cell proliferation between the CS/HEC/GO 10μg and CS/HEC/GO 15μg formulations, indicating comparable cellular viability and growth. Furthermore, our evaluations demonstrated that the selected hydrogel exhibited excellent water absorption and retention properties, as evidenced by the results of the swelling, degradation tests, and *in vitro* Atsttrin release. These characteristics play a pivotal role in ensuring the hydrogel's ability to maintain optimal hydration and stability. These factors are crucial for the hydrogel's overall functionality and its sustained release of Atsttrin over an extended period. SEM analysis revealed no notable variations in the overall morphology between the CS/HEC/GO 10μg and CS/HEC/GO 15μg formulations, indicating similar microstructural features and confirming the absence of significant differences in the material's architecture. In terms of rheology, although the CS/HEC/GO 15μg hydrogel displayed a slightly higher initial storage modulus compared to CS/HEC/GO 10μg, it is important to note that the gelation temperature of CS/HEC/GO 10μg closely matched the physiological body temperature. This characteristic makes the CS/HEC/GO 10μg hydrogel more suitable for practical applications where compatibility with the physiological environment is essential. Based on the results obtained from the *in vitro* study, we have chosen CS/HEC/GO 10μg (herein referred to as "hydrogel") as the most suitable candidate for subsequent *in vitro* and *in vivo* investigations.

3.8. Thermogravimetric (TGA) Analysis

TGA is a widely used technique for investigating the thermal stability and decomposition behavior of materials, including hydrogels. In our study, we utilized TGA Analysis to assess the dry content weight of the hydrogels both with and without Atsttrin, under varying temperatures. This approach provided valuable insights into the thermal properties and degradation patterns of the hydrogel, enabling us to understand the loading content and loading efficiency of Atsttrin within the hydrogel matrix. Through this analysis, we gained important information about the stability and performance of the Atsttrin-loaded hydrogel, contributing to a comprehensive understanding of hydrogel potential as a drug delivery system. The results of TGA analysis are summarized in Table 3, highlighting the changes in weight loss as a function of temperature. The TGA curve, shown in Fig. S4, reveals the thermal degradation profile of the hydrogel and Atsttrin-loaded hydrogel. Within the temperature range of 25–150°C, the weight loss can be observed to occur in three distinct stages. The first stage is characterized by the evaporation of water molecules present in the hydrogel, resulting in an initial weight loss corresponding to the removal of physically adsorbed water and loosely bound water molecules which can occur 25–55 °C in our study. Moving into the second stage, which spans a higher temperature range, the weight loss is attributed to the removal of different functional groups from the hydrogel network. These

functional groups, such as -COOH, -OH, and -NH_2, undergo thermal decomposition and generate volatile byproducts. This stage of weight loss is gradual and signifies the thermal degradation of the hydrogel's chemical constituents in temperature ranging from 55–80 °C, where hydrogel and Atsttrin-loaded hydrogel showed 20.10 and 25.71 % of weight loss values. Finally, in the third stage, the main structure of the hydrogel begins to decompose. This stage is characterized by a significant weight loss as the polymer backbone undergoes degradation, leading to the release of gaseous decomposition products (80–150 °C). The temperature range and extent of weight loss in this stage can provide valuable information about the thermal stability and decomposition behavior of the hydrogel. Interestingly, upon incorporating Atsttrin into the hydrogel, notable differences in the weight loss behavior were observed, particularly within the temperature range of 25–100°C. The hydrogel containing Atsttrin exhibited a higher dry content weight compared to the hydrogel without Atsttrin. This discrepancy suggests that the presence of Atsttrin has an impact on the thermal properties and degradation characteristics of the hydrogel. The higher dry content weight in the Atsttrin-loaded hydrogel may indicate a more effective entrapment of Atsttrin within the hydrogel matrix, potentially attributed to the increased presence of -NH_2, -OH and -COOH groups in the backbone of Atsttrin. These findings contribute to our understanding of the thermal properties of the hydrogel system and guide further optimization and application of Atsttrin-loaded hydrogels in various biomedical and tissue engineering fields.

3.9. Anti-inflammatory effect of Atsttrin

The mRNA expression levels of IL-6 and iNOS were evaluated using qRT-PCR after RAW264.7 cells were stimulated with 10 ng/mL TNF-α for a duration of 24 hours. The analysis demonstrated a significant upregulation of IL-6 expression, with a remarkable fold-change of 3.77 in the RAW264.7 cells treated with TNF-α compared to the control group (Fig. S5). Similarly, the expression level of iNOS exhibited a substantial increase, with a fold-change of 2.84 in the TNF-α treated group (Fig. S5) relative to the control group. In contrast, when RAW264.7 cells were exposed to the hydrogel loaded with Atsttrin, a noticeable reduction in the expression levels of both IL-6 and iNOS was observed. The fold-changes for IL-6 and iNOS were 1.2 and 1.3, respectively, indicating a significant decrease compared to the TNF-α treated group. These findings highlight the potential anti-inflammatory effect of Atsttrin released from the hydrogel. The results suggest that the presence of Atsttrin in the hydrogel formulation exerts a modulatory influence on the pro-inflammatory response triggered by TNF-α, resulting in the downregulation of IL-6 and iNOS gene expression levels in RAW264.7 cells. This implies that Atsttrin has the potential to mitigate the inflammatory cascade induced by TNF-α and restore the balance of pro-inflammatory mediators.

3.10. *In Vitro* Chondrogenesis

In vitro chondrogenesis of bmMSCs using micromass culture system was performed in the presence of chondrogenic media (composed of dexamethasone, ITS, and ascorbic acid) (control group), chondrogenic media + hydrogel alone (hydrogel group), and chondrogenic media + hydrogel loaded with 1000 ng/mL Atsttrin (Atsttrin-loaded hydrogel group) over 10 days. (Fig. 5). Alcian blue staining (Fig. 5a–i) and quantitative assay (Fig. 5j) confirmed GAGs accumulation and occurrence of chondrogenesis in cells cultured in the presence

of the Atsttrin-loaded hydrogels as well as hydrogel group particularly at day 7 and 10 post-incubation, whereas control groups did not show GAGs accumulations density over time. Specific gene expression pattern for chondrogenesis including Col2a1, ACAN, and Sox-9 was carried out by Real-time PCR (Fig. 5k, l, m). Atsttrin released from hydrogel induced the expression of marker genes for chondrogenesis. Expressions of Col2a1 (Fig. 5k), ACAN (Fig. 5l), and Sox-9 (Fig. 5m) were significantly higher in the Atsttrin-loaded hydrogel. Although no significant differences were found between the hydrogel and control groups, the hydrogel group showed higher chondrocyte marker gene expression during 10 days of chondrogenesis (Fig. 5k, l, m).

3.11. *In Vitro* Osteogenesis

Osteogenesis of bmMSCs was assessed in the presence of only osteogenic media (control group), hydrogel + osteogenic media (hydrogel group), and hydrogel loaded with 1000 ng/mL Atsttrin + osteogenic media (Atsttrin-loaded hydrogel group) for 10 days. Alizarin red staining indicates that hydrogel (Fig. 6d, e, f) and Atsttrin-loaded hydrogel (Fig. 6g, h, i) groups enhanced mineral deposition and formed nodular aggregates during 10 days of incubation in comparison to the control group which exhibited minimally alizarin red positive staining (Fig. 6a, b, c). Quantitative analysis showed that compared with the cell group, the hydrogel group showed significantly higher values of calcium matrix deposition, particularly at day 7 and day 10, and the Atsttrin-loaded hydrogel group exhibited the highest value of mineralization over time (Fig. 6j). These results indicate that the calcium deposition in the Atsttrin-loaded hydrogel group distinctly preceded the other groups, while the calcium deposition of the hydrogel group was significantly greater than the control group. For further evaluation, the expressions of osteogenic genes including RUNX-2, BMP-2, osteocalcin (OCL), osteopontin (OCN), ALP, and type I collagen (Col I) were analyzed by qRT-PCR (Fig. 6k,l,m). The highest gene expression levels were detected for the Atsttrin-loaded hydrogel group in comparison to hydrogel and cell groups, suggesting enhanced osteoblast differentiation for this group. On day 3 bmMSCs cultured in the presence of Atsttrin-loaded hydrogel demonstrated the highest induced expressions of RUNX-2 (~3.57 fold) and BMP-2 (3.62 fold) compared to hydrogel and control groups as an early response (Fig. 6k). Further, osteogenesis-related gene expressions of OCL, OCN, ALP, and Col type I for bmMSCs on days 7 and 10 was assessed as the late response (Fig. 6l,m). On day 7, bmMSCs in the presence of Atsttrin-loaded hydrogel demonstrated ~ 6.52, 7.6, 7.07, and 8.15 fold upregulated expressions of OCL, OCN, ALP, and Col I compared to control group (Fig. 6l). Correspondingly, on day 10, cells cultured with Atsttrin-loaded hydrogel revealed the highest expressions of OCL, OCN, ALP and Col I with ~ 7.34, 8.59, 8.71, and 8.3 fold elevation, respectively (Fig. 6m). It is noted that the gene expression levels of the hydrogel group were also significantly higher than those in the control group.

3.12. ALP Staining

To evaluate ALP expression mice bmBMSCs were subjected to a 10-day culture in different conditions including osteogenic medium alone (control group), osteogenic medium with hydrogel (hydrogel group), and osteogenic medium with hydrogel loaded with Atsttrin (Atsttrin-loaded hydrogel group) (Fig. S6). At each time point, the hydrogel and media were discarded first, and then the cells were stained using an ALP staining solution. The

ALP activity of bmBMSCs was initially low on day 3 across all groups, but significantly increased on day 7, with further increases observed on day 10. Importantly, both the hydrogel group and the Atsttrin-loaded hydrogel group exhibited significantly higher ALP activity compared to the control group at all time points. Notably, ALP staining on days 7 and 10 revealed a substantial increase in ALP expression in the Atsttrin-loaded hydrogel group compared to the hydrogel group. Moreover, semi-quantitative analysis confirmed that ALP expression was significantly stronger in the Atsttrin-loaded hydrogel group. Specifically, the ALP activity in bmMSCs in the Atsttrin-loaded hydrogel group was 2-fold higher than that in the control group, for each time point. Significant differences were found between control and hydrogel groups. These findings collectively demonstrate that both the hydrogel and Atsttrin promoted the differentiation of bmBMSCs into osteoblasts. This conclusion is consistent with the results obtained from Alizarin Red staining (Fig.6 a–j), which revealed a significant enhancement in calcium deposition over time, particularly in the Atsttrin-loaded hydrogel group at 7 and 10 days.

3.13. *In Vivo* Study

3.13.1. Histology Evaluation—Diabetic mice were subjected to a closed gravity fracture model followed by the injection of PBS (10 μL of sterile PBS) (control group), hydrogel (10 μL of hydrogel without Atsttrin), and hydrogel loaded with Atsttrin (8 μg of Atsttrin/10 μL of hydrogel) at the fracture site immediately after establishing the fracture. Histology evaluation using Safranin/O Fast green (Fig. 7) and Pentachrome staining (Fig. S7) demonstrated accelerated diabetic fracture healing in Atsttrin-loaded hydrogel treatment compared to other groups. In all groups a large callus tissue formed by day 10 post-surgery (Fig. 7a, d, g, Fig. S7a, d, g). On day 16 post-fracture, the Atsttrin-loaded hydrogel-treated mice showed decreased callus and unmineralized cartilage and increased newly formed bone relative to hydrogel and PBS groups (Fig. 7h, Fig. S7h). In addition, the bone gap between the ends of the femur at the fracture site was almost healed. On day 21, the bone gap at the fracture site was filled by bone minerals and completely healed, and the bone started remodeling and returned to normal geometries. At this point in time, no callus nor residual bone gap was observed at the fracture site in the Atsttrin-loaded hydrogel treated mice compared with hydrogel alone and PBS-treated mice (Fig. 7i, Fig. S7i). For the hydrogel-treated mice, callus tissue and, lower amounts of newly formed bone tissue were observed at 16 days post-fracture compared to the Atsttrin-loaded hydrogel-treated mice at this time point; however, the size of the callus decreased in comparison to that on day 10 post-fracture (Fig. 7e, Fig. S7e). On day 21 post-surgery a slight amount of callus was observed, bone was healing, and the bone gap almost closed (Fig. 7f, Fig. S7f). In the PBS-treated group, the callus tissue was observed during the entire fracture healing process. Although, the size of the callus was reduced by day 21 post-surgery mice in this group, a larger callus area was observed compared to the other treatment group on day 16 (Fig. 7b, Fig. S7b). On day 21 following the bone fracture, we observed a little appreciable bone development, callus was still observed, and the bone gap at the fracture site did not close and remained open with almost no sign of clear bony bridge formation (Fig. 7c, Fig. S7c).

3.13.2. MicroCT Analysis—The femur tissues were harvested, surrounding soft tissues removed and fixed in 4 % PFA for 48 hours (Fig. S8). MicroCT analysis was employed

on T1DM femurs fracture to evaluate changes in mice bone quality at day 21 post-fracture (Fig. 8). MicroCT analysis revealed a partial large fracture callus in 3D images of the PBS group. Femur fracture callus in this group remained less advanced with a transverse gap in the center of femur diaphysis, indicating the bony bridge of the fracture site was incomplete (Fig. 8A). At the same time, the hydrogel-treated mice displayed an almost completed bony bridge between neighboring femur fracture ends at the fracture site. Atsttrin-loaded hydrogel treatment exhibited a-complete-bony-bridge at fracture site that was entirely integrated with the adjacent femur ends. The callus area in the fracture site of the femoral bone was filled with the new bone; however, it was nearly empty for the PBS group. Bone microarchitectural parameters including, bone mineral density (BMD), tissue mineral density (TMD), bone volume fraction (BV/TV, %), trabecular thickness (Tb.th), trabecular number (Tb. N), and trabecular spacing (Tb.S) values were analyzed for the region of interest of the fracture site (Fig. 8B). Histomorphometry analysis of the region of interest at the fracture site on day 21 post-surgery indicated significant improvement of TMD, BMD, and BV/TV values in Atsttrin-loaded hydrogel group followed by the hydrogel group (Fig. 8B). The amount of new bone tissues formed in the Atsttrin-loaded hydrogel group were significantly higher than those in the hydrogel and PBS treated groups. As shown in Fig. 8B, less amount of newly formed bone was observed in the PBS group at day 21 post-fracture, and TMD, BMD, and BV/TV showed even lower values than in the hydrogel group. In addition, the PBS group exhibited significantly lower Tb.th and Tb. N values compared to those in the hydrogel and Atsttrin-loaded hydrogel groups. In contrast, Tb.S was decreased and showed the lowest value in the Atsttrin-loaded hydrogel group, while it showed the highest value in the PBS group, indicating that combination of hydrogel and Atsttrin had the greatest ability to promote *in vivo* bone fracture healing effectively by enhancing the callus formation and the subsequent bone remodeling process.

3.13.3. Nanoindentation test—Of the 99 nanoindentations curves, nine were excluded due to contact problems. A total of 90 nanoindentations were analyzed (72 on cortical bone and 18 on the trabecular bone) to evaluate the mechanical strength of newly formed bone in the experimental and control group at 3 weeks post-surgery (Fig. 9, Fig. S9). For cortical bone, significant differences were found in modulus among all groups. Similar trends were found for hardness in all groups. The results indicated that the cortical bone of mice treated with Atsttrin-loaded hydrogel and hydrogel was found to be significantly stiffer (8.65 GPa, 6.99 GPa) and harder (0.43GPa, 0.37 GPa) than those of mice treated with PBS (8.43 GPa, 0.28 GPa). In trabecular bone, significant differences were found in stiffness and hardness between mice treated with PBS (2.23 GPa, 0.1 GPa) and mice treated with hydrogel (2.91 GPa, 0.13 GPa) and Atsttrin-loaded hydrogel (2.94 GPa, 0.14 GPa). Although the stiffness and hardness in the Atsttrin-loaded hydrogel showed higher values than that in the hydrogel group in trabecular bone, no significant differences were found between the hydrogel and Atsttrin-loaded hydrogel groups. Overall, the results of the nanoindentation test showed that Atsttrin-loaded hydrogel-treated fractures presented earlier endochondral ossification, accelerated bone formation and mineralization, and faster bone healing, which are consistent with the obtained results from histology and microCT analysis (Figs. 7, 8). Nevertheless, accelerated bone regeneration and remodeling, and overall bone strength were found to be significantly increased in Atsttrin-loaded hydrogel compared to hydrogel and PBS groups.

3.13.4. Bulk RNA-Seq and Gene Set Enrichment Analysis—As shown in Fig.10, GSEA analysis revealed that inflammatory pathways such as interferon-gamma (IFN- **γ**) mediated signaling pathway, IL-1, and 5 mediated pathways, T-cell activation, and positive regulation of acute inflammatory response were largely downregulated in Atsttrin-loaded hydrogel group compared to those of PBS and hydrogel treated groups. Interestingly, GSEA analysis indicated that proteoglycan biosynthetic processes, cartilage development, endochondral bone morphogenesis, regulation of BMP signaling, and regulation of cellular response to TGF- ▯ signaling pathways were upregulated in Atsttrin-loaded hydrogel compared to those in other groups. In contrast, we observed upregulated signaling pathways such as adaptive immune response, natural killer cell-mediated immunity, and myeloid leukocyte mediated immunity in hydrogel and PBS groups (Fig. 10, Fig. S10). The common differentially regulated genes, known to be associated with the inflammatory mediated signaling as well as chondrogenesis and osteogenesis, among the Atsttrin-loaded hydrogel, hydrogel, and PBS-treated groups at different time points post-surgery are shown in Fig. S11.

3. Discussion

The objective of this study was to evaluate the therapeutic effects of combining Atsttrin with a CS/HEC/GO hydrogel in the treatment of closed gravity-induced femur fractures in a mouse model with T1DM. To achieve this, we employed a thermoresponsive injectable hydrogel that offers several advantages over traditional grafts or surgical hardware, including controlled and sustained release of Atsttrin and the avoidance of invasive surgical procedures [47]. The CS/HEC/GO/β-GP hydrogel, used as a carrier for Atsttrin, exhibits notable benefits such as biocompatibility, the absence of toxicity, and the generation of non-toxic degradation byproducts. Furthermore, this hydrogel possesses a well-defined composition and structure, ensuring its reliability and efficacy [48]. Importantly, the injectable nature of the hydrogel enables localized delivery of Atsttrin, leading to higher concentrations at the fracture site for an extended duration of time. By utilizing the CS/HEC/GO hydrogel as a controlled-release system, we aimed to create an optimal environment for the sustained and targeted delivery of Atsttrin, thus maximizing its therapeutic potential in promoting fracture healing. This innovative approach has the potential to revolutionize the treatment of femur fractures in individuals with T1DM, offering improved outcomes while minimizing the invasiveness and risks associated with conventional surgical procedures.

The reaction between GO with CS and HEC during crosslinking as illustrated in Fig. 1 results in the formation of electrostatic interactions. The positive amino groups of CS interact with the negative charge groups of GO and HEC resulting in the stabilization of the hydrogel structure [53]. The addition of GO leads to a reduction in gelation temperature as depicted in Fig. 2. This can be attributed to the individual crosslinking of CS, as well as HEC and CS/HEC, with the GO sheets. Under acetic acid condition, pH levels below 6.5, electrostatic interactions occur between the negative and positive functional groups of materials, facilitated by the polycationic nature of CS [56]. In addition, the hydrogen bonding between the oxygen-containing groups and amino groups in the backbone of CS are involved in sol-gel transition [53, 57]. Moreover, the electrostatic interaction between the negative phosphate groups of β-GP and the positive $-NH_2^+$ groups of CS lead to a

decrease in the ratio of cationic and anionic functional groups in CS and β-GP, respectively. As a result, the repulsion between protonated groups in CS is weakened [58] and the hydrophobic effect becomes dominant, playing a significant role in the formation of a 3D gel network [58–61]. In the presence of GO sheets, the hydrophobic effect is further reinforced, promoting stronger entanglement of polymer chains and consequently inducing faster sol-gel formation [60, 62]. These findings align with previous studies that have reported accelerated gelation process in hydrogels containing GO [53, 60]. Overall, the results obtained in this study provide further support for the role of GO in facilitating the efficient and rapid gelation of the hydrogel system. Additionally, the hydrogels containing higher concentrations of GO demonstrated a notable increase in the initial storage modulus compared to the GO-free hydrogel. This observation suggests that the incorporation of GO into the hydrogel formulation enhances its chemical properties and provides greater stability (Fig. 2).

The impact of GO on the swelling and degradation behavior of the hydrogel was also assessed in this study. As observed in the swelling and degradation rate analysis (Fig. 3a,b), the incorporation of GO resulted in distinct patterns for swelling and degradation for GO incorporating hydrogels compared to the control group. The increased number of interactions between positive and negative functional groups, along with the strengthened hydrogen bonding and hydrophobic effect between GO and the polymer matrix, and the constrained movement of water molecules within the hydrogel contributed to a more compact and dense network structure [62]. This structural arrangement limited the penetration of water molecules and degrading agents, leading to a slower swelling and degradation process. The hydrogels containing GO exhibited a relatively lower swelling rate and slower degradation rate, indicative of their enhanced stability and prolonged structural integrity over time.

Furthermore, the controlled release of Atsttrin from the hydrogel is also influenced by the presence of GO (Fig. 3c,d) The higher concentration of GO in the hydrogel formulation enhances the hydrophobic effect, further impeding the diffusion of Atsttrin molecules and reducing the release rate [63–66]. These findings are also in accordance with and confirm the rheology test results, where addition of GO leads to reduced gelation temperature (Fig. 2). The reduced gelation temperature indicates that GO accelerates the gelation process, resulting in a more rapid transition from sol to gel state. The findings presented in this study offer further support for the structural and functional properties of the hydrogel system, establishing it as a suitable carrier for the loading of Atsttrin. This was confirmed by TGA, which revealed distinct weight loss values for CS/HEC/GO 10 μg loaded with Atsttrin compared to the hydrogel without Atsttrin (Fig. S4 and Table 3). The observed differences in weight loss at the same temperature strongly indicate the presence of Atsttrin within the hydrogel, which is characterized by a higher concentration of -OH and -NH_2 functional groups. These results signify the successful incorporation of Atsttrin into the hydrogel network. Consequently, this study provides compelling evidence for the efficient entrapment and retention of Atsttrin within the hydrogel matrix, underscoring the potential of the hydrogel as a stable carrier for this therapeutic agent.

MTT assay results demonstrated excellent cell viability with no toxicity observed after 24 hours of incubation, as indicated by a cell viability higher than 85.5% (Fig. 3e). Furthermore, the MTT assay revealed a higher proliferation rate for all hydrogels containing GO compared to the hydrogel without GO, highlighting the positive influence of GO on cell growth and proliferation (Fig. 3f).

The selection of hydrogel composition is of utmost importance in promoting cell growth and achieving desired tissue regeneration outcomes. In our study, we employed a carefully chosen combination of CS, HEC, β-GP and GO to construct the hydrogel. These specific materials were selected based on their well-established biocompatibility and bioactivity, which are known to support cell proliferation and differentiation. The degradation products derived from the CS, HEC, and β-GP used in our study, exhibit bioactive properties that have been reported to influence various aspects of cellular behavior, including cell growth, proliferation, and differentiation [31, 67–72]. GO has emerged as a versatile and promising material across various scientific disciplines, primarily due to its exceptional properties such as large surface area, high mechanical strength, and excellent electrical conductivity. Numerous studies have reported the ability of GO to enhance cell adhesion, proliferation, and differentiation by interacting with cells and modulating key cellular signaling pathways [2, 26, 27, 73, 74]. However, concerns regarding the potential toxicity of GO, particularly in a dose-dependent manner, have been raised. Previous research has demonstrated that GO concentrations exceeding 50 μg/mL can induce cytotoxicity and inhibit cell proliferation [75, 76]. Consistent with these findings, our study investigated the effect of various concentrations of GO ranging from 10 μg/mL to 60 μg/mL on cell viability (Fig. S3). Notably, we observed a concentration-dependent effect, particularly at higher concentrations of 50 μg/mL and 60 μg/mL, where a significant decrease in cell viability was evident.

Based on the obtained results from MTT assay regarding GO cytotoxicity, we utilized a relatively low concentration of GO, up to 15 μg/mL, for the fabrication of hydrogels. Hence, based on our observations, it can be inferred that the slight decrease in the proliferation rate of bmMSCs with the CS/HEC/GO 15 μg hydrogel may not be attributed to the cytotoxicity of GO. This conclusion is supported by the fact that bmMSCs still exhibited a substantial and higher proliferation rate in comparison to the control group. Additionally, no statistically significant differences were observed between the CS/HEC/GO 15 μg hydrogel and other hydrogels containing lower concentrations of GO. Overall, our findings indicate that at the concentration used in the current study, GO did not exhibit significant cytotoxic effects on cell viability. However, further investigations are required to comprehensively understand the dose-dependent toxicity of GO and its precise impact on cellular behavior in the context of specific applications.

SEM imaging revealed notable significant differences between the hydrogel samples containing GO and the control group, as shows in Fig. 4. The incorporation of GO resulted in smaller pore size and thicker pore walls compared to the control group. This can be attributed to the increased number of interactions between the positive and negative functional groups upon the addition of GO to the gelling solution. The presence of GO not only enhances the formation of electrostatic interactions but also strengthens hydrogen bonding interactions [60].

Additionally, the hydrophobic effect between the phosphate group of β-GP and the amine group of CS further contributes to the constraints on the free movement of water molecules within hydrogels. Because of these interactions, the resistance to the formation of larger ice crystals during the freeze-drying process is enhanced. This leads to reduction in pore size within the hydrogels, as observed in the SEM images. The smaller pore size and thicker pore walls observed in the SEM images of the hydrogels with GO can also be linked to their reduced swelling and degradation rate. The smaller pore size, in turn, influences the swelling rate of the hydrogels (Fig. 3a). The reduced pore size hinders the rapid uptake of water, resulting in a slower swelling and subsequently degradation rate [72].

Chondrogenesis assessments showed *in vitro* chondrocyte differentiation of bmMSCs for Atsttrin-loaded hydrogel and partial differentiation for hydrogel groups (Fig. 5). This outcome aligns with a previous report demonstrating that Atsttrin promotes *in vitro* chondrogenesis of mouse MSCs [39]. It has been well-documented that certain components of the ECM derived from cartilage, such as GAGs, play a crucial role in supporting chondrogenesis [77]. In this study, CS, a positively-charged natural polysaccharide polymer, has a molecular structure similar to that of GAGs, which makes it extensively employed as a biocompatible material for cartilage regeneration [78, 79]. Previous investigations have demonstrated that CS enhances *in vitro* chondrogenic differentiation capability of MSCs without applying exogenous chemical factors [80–82]. Additionally, the utilization of HEC holds significant promise as a platform for cartilage regeneration [83–85]. A notable finding of the current study is that both CS and HEC, the materials incorporated in hydrogels, possess the capacity to induce chondrogenic differentiation of bmMSCs up to a certain level even without the requirement of specialized culture conditions during a 10-days of incubation period (Fig. 5).

In addition, our investigation has revealed a distinct temporal expression pattern of chondrocyte markers during the culture period, shedding valuable light on the influence of Atsttrin-loaded hydrogel on chondrogenesis. Initially, we observed a significant upregulation of these markers, which can be attributed to the higher initial release of Atsttrin from the hydrogel. Specifically, the calculated release at the beginning of the culture period was 10.10% for CS/HEC/GO 10 μg hydrogel (Fig. 3c,d). This release acted as a stimulant for chondrogenesis, resulting in an intensified expression of chondrogenesis markers and a heightened alcian blue staining response. As the culture period progressed over the course of 10 days, we noticed a gradual increase in gene expression, indicating the sustained impact of Atsttrin's controlled-release properties. This gradual elevation in chondrogenesis markers signifies the continuous promotion of chondrogenesis throughout the entire culture duration.

The deposition of calcium observed in all groups, particularly in the Atsttrin-loaded hydrogel and hydrogel groups, serves as a noteworthy indicator of successful *in vitro* bone formation (Fig. 6). Our findings align with previous studies that have reported the significant enhancement of calcium deposition and osteogenic gene expression in bmMSCs cultured on GO-based substrates, both in normal and osteogenic media [86–88]. Although GO has been employed as a potential nanoplatform for bone tissue engineering application, several aspects regarding its interactive mechanism with cells, and its *in vivo* bone-forming ability, are still remain unknown. Researchers have hypothesized that osteogenesis capability of GO

might be due to the presence of the hydrophobic domains on the surface of GO sheets, along with ionized functional groups around the GO edges [27, 89]. These hydrophobic and ionized functional groups create a unique nanotopography and provide effective environments that promoting cell functions through the electrostatic and hydrophobic interactions with various molecules. Consequently, these interactions have the potential to improve cellular behaviors and promote the *in vitro* osteogenic differentiation [86, 90, 91].

Significantly, β-GP, an integral component of the hydrogel formulation, has been emerged as a pivotal factor in driving the osteogenesis process. Previous studies have reported the crucial role of β-GP in promoting osteogenesis, with ALP being implicated in this process [30, 92]. Consistent with these reports, our investigation utilized alizarin red staining to detect calcium deposition and ALP staining to assess ALP expression (Fig. S6). These analyses provided further compelling evidence of the active involvement of ALP in mediating the osteogenic differentiation of bmMSCs along with β-GP. ALP, recognized as a key marker of early osteogenic differentiation, plays a vital regulatory role in the mineralization process and the formation of bone tissue [92]. Our findings underscore the successful induction of osteogenesis, even at the early time point of 3 days, particularly for the Atsttrin-loaded hydrogel group followed by the hydrogel group. Hence, our results are in line with the previous studies where successful detection of mineralization at day 3 have been reported [93–95]. The positive outcomes observed can be attributed to the presence of Atsttrin, GO, β-GP, and potentially other components within the hydrogel formulation. These results indicate that hydrogel in combination with Atsttrin stimulated both chondrogenic and osteogenic differentiation of bmMSCs much more potently than with hydrogel alone and cell groups during 10 days of incubation, suggesting the synergistic effects between the biomaterials used in the hydrogel and Atsttrin in regulating chondrogenic and osteogenic differentiation.

After 3 weeks of fracture (Figs. 7, 8, and 9), PBS and hydrogel-treated mice displayed diminished fracture healing in comparison to Atsttrin-loaded hydrogel groups. However, this reduced bone fracture healing was more prominent in diabetic treated-PBS mice where diabetes significantly delayed fracture healing in this group. It has been demonstrated that DM contributes to increased bone fracture risk and bone healing impairment by reducing BMD, which is a major complication of individuals with diabetes [96, 97]. Pro-inflammatory cytokines including TNF-α, IL-1β, and IL-6 are increased locally in DM and are thought to contribute to diabetic complications and play an essential role in impaired bone healing [98]. Among pro-inflammatory cytokines, TNF-α is known as a major inflammatory cytokine and at the apex of the inflammatory cascade. TNF-α is mainly secreted by inflammatory cells in diabetes at the fracture site and impedes fracture healing by chondrocyte apoptosis [96, 99]. Given the role of TNF-α in the pathogenesis of diabetic fracture healing, targeted regulation of TNF-α signaling with novel anti-inflammatory molecules can offer an excellent opportunity to develop the biologics for improvement of the impaired fracture healing under diabetic conditions. This strategy has been proved to be successful in the treatment of many inflammatory diseases such as DM. One such candidate is Atsttrin, a PGRN derivative, well known for its anti-inflammatory and chondrogenic properties [39, 44–46].

Consistent with previous data, our findings demonstrate that Atsttrin exerts a significant reduction in the levels of IL-6 and iNOS in RAW264.7 cells treated with 10 ng/mL TNF-α following 24 hours of incubation (Fig. S5). This observation aligns with earlier studies that have reported anti-inflammatory properties of Atsttrin, specifically its ability to modulate the production of pro-inflammatory cytokines and mediators in response to TNF-α stimulation. By inhibiting the expression and release of inflammatory cytokine, Atsttrin exhibits promising potential as a therapeutic agent for mitigating TNF-α-induced inflammation and associated pathologies.

It was reported that both PGRN and Atsttrin exert their therapeutic/protective effects by inhibiting TNFα/TNFR1 inflammatory and catabolic and activating TNFR2 anti-inflammatory and regenerative pathways [3, 38, 39, 44, 45, 100–103].

In our study the combined therapy of Atsttrin and hydrogel demonstrated significant potential in promoting cartilage regeneration and bone fracture healing in diabetes through the modulation of key signaling pathways and suppression of inflammatory responses. Through the utilization of bulk RNA-Seq analysis, we were able to gain further insight into the intricate molecular mechanisms that underlie bone regeneration and the enhanced healing of diabetic fractures when treated with a combination of Atsttrin and injectable hydrogel. These findings shed light on the promising potential of this therapeutic approach for future applications in bone fracture healing. The comprehensive transcriptomic analysis enabled us to elucidate the specific genes and pathways involved in the beneficial effects observed, providing a deeper understanding of the intricate biological processes at play. This valuable knowledge contributes to the ongoing efforts in advancing treatment strategies for diabetic fracture healing and holds significant promise for the development of innovative therapeutic interventions in the field of bone regeneration (Fig. 10, Figs. S10,11).

One of the key findings in our study was the stimulation of chondrogenesis and osteogenesis, which are essential processes for cartilage regeneration and bone healing. The upregulation of genes such as Col 2a1, Sox 9, COMP, TGF β2, TGF β3, Col 1a, BMP 2, FGF 18, and BMP10 indicates enhanced tissue regeneration potential and supports the efficacy of the combined therapy (Fig. S11). [49, 104–111]. These genes are known to play crucial roles in chondrocyte differentiation, cartilage development, endochondral bone morphogenesis, and response to BMP and TGF β signaling pathways [112, 113]. By promoting the expression of these genes, the therapy creates a favorable environment for tissue repair and regeneration. Furthermore, the downregulation of inflammatory markers is important in promoting tissue healing. Inflammatory pathways, including IL-1, IL-6, complement components, IFN-γ, IFN-α2, NF-κB, MAPK, and Wnt5a, are known to hinder the regenerative process [114–116]. The observed suppression of these markers suggests that the combined therapy effectively attenuates the inflammatory cascade, allowing for an optimal environment for tissue regeneration. By modulating these pathways, the therapy mitigates the negative impact of inflammation on cartilage and bone healing. Our study also highlights the involvement of key growth factors and signaling molecules in the therapeutic response. BMP-2, a potent morphogen, plays a crucial role in stimulating bone formation and enhancing vascularized bone regeneration at fracture sites [109]. The upregulation of BMP-2 expression further supports the regenerative potential of

the therapy. Additionally, the downregulation of Wnt5a, a non-canonical Wnt ligand, is consistent with previous studies showing that BMPs downregulate Wnt signaling during osteogenic differentiation. The inhibition of Wnt5a and subsequent downregulation of Wnt signaling contribute to enhanced osteogenesis and bone healing by inhibiting the osteoclast precursors differentiation and activation [117–122]. The remarkable suppressive effects of the combined therapy on IL-1 and IL-6 are highly noteworthy. Previous studies have reported that IL-1β, by activating NF-κB and MAPK signaling pathways, negatively regulates BMP signaling and osteogenesis [115]. By downregulating IL-1 expression, our therapy effectively counteracts its inhibitory effects, leading to improved bone healing. Furthermore, IL-6 has been recognized for its ability to enhance osteoclast differentiation, which can impede the bone healing process [116]. Remarkably, our therapy successfully downregulates IL-6 expression, thereby reducing its impact on osteoclastogenesis and promoting bone regeneration.

It is important to note that the therapy's success in promoting tissue regeneration and modulating inflammatory and signaling pathways highlights the potential for future advancements in bone regeneration treatments. However, further investigation is warranted to fully elucidate the underlying mechanisms mediating the regenerative effects and the intricate interactions between Atsttrin, hydrogel, and the signaling pathways involved. This will enable a more comprehensive understanding of the therapy's mode of action and guide the development of optimized treatment approaches. Our study demonstrates that the combined therapy of Atsttrin and hydrogel holds a promise in promoting cartilage regeneration and bone healing. Through the modulation of key signaling pathways and suppression of inflammatory responses, the therapy creates an environment conducive to tissue repair and regeneration. These findings contribute to the growing body of knowledge in the field of bone regeneration and provide valuable insights for the development of effective therapeutic strategies. Continued research in this area will pave the way for improved treatments and better clinical outcomes in bone regeneration.

Taken together, this study provides groundbreaking insights into the role and mechanisms of Atsttrin in combination with hydrogel in healing diabetic bone fractures. It holds tremendous promise for developing innovative therapeutic interventions, specifically tailored to address impaired fracture healing, especially in diabetic bone fractures. During the experiment, we physically blended Atsttrin with hydrogel components, resulting in gel formation at 37 °C, and meticulously assessed the hydrogel's stability. This process effectively entrapped and retained Atsttrin within the hydrogel structure, potentially enabling controlled drug release. Looking ahead, we acknowledge the importance of conducting comprehensive *in vitro* studies to investigate the interaction between the hydrogel component and Atsttrin. Furthermore, conducting *in vivo* investigations will deepen our understanding of the hydrogel's performance, stability, and its potential for sustained gel formation within living system. It is worth to note that, according to our previous experiences in the field of diabetic fracture healing, we exercised careful consideration and chose three pivotal time points for *in vivo* study: day 10, day 16, and day 21, to meticulously examine the intricate healing process. Each of these time points holds immense importance in unraveling the dynamic interplay of biological events that transpire during the recovery phase of diabetic bone fractures. While these selected time points offer invaluable insights into the progression of

healing, we recognize the potential for even greater understanding by exploring an additional time point at day 7. Incorporating this time point in our investigation could potentially provide crucial *in vivo* information on the early stages of the healing process, shedding light on the initial effects of our constructs on osteogenesis and the overall diabetic fracture healing trajectory.

4. Conclusion

Similar to PGRN, a secreted growth factor-like molecule known to be important in chondrogenesis during development and regenerative processes [39, 123], PGRN-derived Atsttrin also promotes chondrogenesis and bone fracture healing [39, 123]. The current study demonstrates, for the first time, that Atsttrin in combination with CS/HEC/GO hydrogel exerts a significant therapeutic effect on callus formation and subsequent bone mineralization and bone regeneration in type 1 diabetic fracture healing model. This study not only provides novel insights into the role and mechanism of Atsttrin in diabetic bone fracture healing, but may also lead to the development of novel and promising therapeutic intervention strategies for variety of the impaired fracture healing, in particular, diabetic bone fracture healing.

Supplementary Material

Refer to Web version on PubMed Central for supplementary material.

Acknowledgements

This work was supported partly by NIH research grants R01AR076900, R01AR062207, R01AR061484, R01AR078035 and R01NS070328.

References

1. Ceriello A, Monnier L, and Owens D, Glycaemic variability in diabetes: clinical and therapeutic implications. The lancet Diabetes & endocrinology, 2019. 7(3): p. 221–230. [PubMed: 30115599]
2. Alblowi J, et al. , Chemokine expression is upregulated in chondrocytes in diabetic fracture healing. Bone, 2013. 53(1): p. 294–300. [PubMed: 23262028]
3. Wei J, et al. , Progranulin promotes diabetic fracture healing in mice with type 1 diabetes. Annals of the New York Academy of Sciences, 2020. 1460(1): p. 43–56. [PubMed: 31423598]
4. Ceriello A and Kilpatrick ES, Glycemic variability: both sides of the story. Diabetes Care, 2013. 36(Suppl 2): p. S272. [PubMed: 23882058]
5. Hu Z, et al. , Immunomodulatory ECM-like microspheres for accelerated bone regeneration in diabetes mellitus. ACS applied materials & interfaces, 2018. 10(3): p. 2377–2390. [PubMed: 29280610]
6. Kayal RA, et al. , Diabetes causes the accelerated loss of cartilage during fracture repair which is reversed by insulin treatment. Bone, 2009. 44(2): p. 357–363. [PubMed: 19010456]
7. Tam RY, et al. , Rationally Designed 3D Hydrogels Model Invasive Lung Diseases Enabling High-Content Drug Screening. Advanced Materials, 2019. 31(7): p. 1806214.
8. Zhang K, et al. , Adaptable hydrogels mediate cofactor-assisted activation of biomarker-responsive drug delivery via positive feedback for enhanced tissue regeneration. Advanced Science, 2018. 5(12): p. 1800875. [PubMed: 30581701]
9. Hu S, et al. , A mussel-inspired film for adhesion to wet buccal tissue and efficient buccal drug delivery. Nature communications, 2021. 12(1): p. 1689.

10. Wang T, et al. , Sodium alginate hydrogel containing platelet-rich plasma for wound healing. Colloids and Surfaces B: Biointerfaces, 2023. 222: p. 113096. [PubMed: 36542954]
11. Chen Z, et al. , Injectable wound dressing based on carboxymethyl chitosan triple-network hydrogel for effective wound antibacterial and hemostasis. International Journal of Biological Macromolecules, 2023. 225: p. 1235–1245. [PubMed: 36435472]
12. Hermenean A, et al. , The impact of graphene oxide on bone regeneration therapies. Advanced Techniques in Bone Regeneration, 2016: p. 151–167.
13. Stancu I, Lungu A, and Iovu H, Hydrogels for bone regeneration, in Biomaterials for Bone Regeneration. 2014, Elsevier. p. 62–86.
14. Gómez S, et al. , Design and properties of 3D scaffolds for bone tissue engineering. Acta biomaterialia, 2016. 42: p. 341–350. [PubMed: 27370904]
15. Levengood SKL and Zhang M, Chitosan-based scaffolds for bone tissue engineering. Journal of Materials Chemistry B, 2014. 2(21): p. 3161–3184. [PubMed: 24999429]
16. Roseti L, et al. , Scaffolds for bone tissue engineering: state of the art and new perspectives. Materials Science and Engineering: C, 2017. 78: p. 1246–1262. [PubMed: 28575964]
17. Amini AR, Laurencin CT, and Nukavarapu SP, Bone tissue engineering: recent advances and challenges. Critical Reviews™ in Biomedical Engineering, 2012. 40(5).
18. Black CR, et al. , Bone tissue engineering. Current molecular biology reports, 2015. 1: p. 132–140. [PubMed: 26618105]
19. Tozzi G, et al. , Composite hydrogels for bone regeneration. Materials, 2016. 9(4): p. 267. [PubMed: 28773392]
20. Geckil H, et al. , Engineering hydrogels as extracellular matrix mimics. Nanomedicine, 2010. 5(3): p. 469–484. [PubMed: 20394538]
21. Xu X, et al. , Chitosan-based multifunctional hydrogel for sequential wound inflammation elimination, infection inhibition, and wound healing. International Journal of Biological Macromolecules, 2023. 235: p. 123847. [PubMed: 36863672]
22. Cho MH, et al. , Chitosan gel as an in situ–forming scaffold for rat bone marrow mesenchymal stem cells in vivo. Tissue Engineering Part A, 2008. 14(6): p. 1099–1108. [PubMed: 19230130]
23. Croisier F and Jérôme C, Chitosan-based biomaterials for tissue engineering. European polymer journal, 2013. 49(4): p. 780–792.
24. Saeedi M, et al. , Customizing nano-chitosan for sustainable drug delivery. Journal of Controlled Release, 2022. 350: p. 175–192. [PubMed: 35914615]
25. Bharathi R, et al. , Chitosan-based scaffolds as drug delivery systems in bone tissue engineering. International Journal of Biological Macromolecules, 2022.
26. Amiryaghoubi N, et al. , Recent advances in polymeric scaffolds containing carbon nanotube and graphene oxide for cartilage and bone regeneration. Materials Today Communications, 2021. 26: p. 102097.
27. Choe G, et al. , Graphene oxide/alginate composites as novel bioinks for three-dimensional mesenchymal stem cell printing and bone regeneration applications. Nanoscale, 2019. 11(48): p. 23275–23285. [PubMed: 31782460]
28. Chahal S, et al. , Electrospun hydroxyethyl cellulose nanofibers functionalized with calcium phosphate coating for bone tissue engineering. RSC advances, 2015. 5(37): p. 29497–29504.
29. Bakhiet E, Jauhari NFIM, and Zulkifli FH. Biomineralization of Hydroxyethyl Cellulose/Sodium Alginate for Bone Tissue. in Materials Science Forum. 2021. Trans Tech Publ.
30. Shioi A, et al. , β-Glycerophosphate accelerates calcification in cultured bovine vascular smooth muscle cells. Arteriosclerosis, thrombosis, and vascular biology, 1995. 15(11): p. 2003–2009. [PubMed: 7583582]
31. Wang C, Cao X, and Zhang Y, A novel bioactive osteogenesis scaffold delivers ascorbic acid, β-glycerophosphate, and dexamethasone in vivo to promote bone regeneration. Oncotarget, 2017. 8(19): p. 31612. [PubMed: 28404942]
32. Ding H, et al. , Progranulin derived engineered protein Atsttrin suppresses TNF-alpha-mediated inflammation in intervertebral disc degenerative disease. Oncotarget, 2017. 8(65): p. 109692–109702. [PubMed: 29312639]

33. Fu W, Hettinghouse A, and Liu CJ, In Vitro Physical and Functional Interaction Assays to Examine the Binding of Progranulin Derivative Atsttrin to TNFR2 and Its Anti-TNFalpha Activity. Methods Mol Biol, 2021. 2248: p. 109–119. [PubMed: 33185871]
34. Liu C, et al. , Progranulin-derived Atsttrin directly binds to TNFRSF25 (DR3) and inhibits TNF-like ligand 1A (TL1A) activity. PLoS One, 2014. 9(3): p. e92743. [PubMed: 24651300]
35. Wei JL, et al. , Progranulin derivative Atsttrin protects against early osteoarthritis in mouse and rat models. Arthritis Res Ther, 2017. 19(1): p. 280. [PubMed: 29258611]
36. Zhao YP, Tian QY, and Liu CJ, Progranulin deficiency exaggerates, whereas progranulin-derived Atsttrin attenuates, severity of dermatitis in mice. FEBS Lett, 2013. 587(12): p. 1805–10. [PubMed: 23669357]
37. Cui Y, Hettinghouse A, and Liu CJ, Progranulin: A conductor of receptors orchestra, a chaperone of lysosomal enzymes and a therapeutic target for multiple diseases. Cytokine Growth Factor Rev, 2019. 45: p. 53–64. [PubMed: 30733059]
38. Feng JQ, et al. , Granulin epithelin precursor: a bone morphogenic protein 2-inducible growth factor that activates Erk1/2 signaling and JunB transcription factor in chondrogenesis. The FASEB Journal, 2010. 24(6): p. 1879–1892. [PubMed: 20124436]
39. Wei J, et al. , Atsttrin promotes cartilage repair primarily through TNFR2-Akt pathway. Frontiers in cell and developmental biology, 2020. 8: p. 577572. [PubMed: 33195216]
40. Wei J. l., et al. , Progranulin derivative Atsttrin protects against early osteoarthritis in mouse and rat models. Arthritis research & therapy, 2017. 19(1): p. 1–14. [PubMed: 28073368]
41. Feng JQ, et al. , Granulin epithelin precursor: a bone morphogenic protein 2-inducible growth factor that activates Erk1/2 signaling and JunB transcription factor in chondrogenesis. The FASEB Journal, 2010. 24(6): p. 1879. [PubMed: 20124436]
42. Cui Y, Hettinghouse A, and Liu C.-j., Progranulin: a conductor of receptors orchestra, a chaperone of lysosomal enzymes and a therapeutic target for multiple diseases. Cytokine & growth factor reviews, 2019. 45: p. 53–64. [PubMed: 30733059]
43. Liu C. j., Progranulin: a promising therapeutic target for rheumatoid arthritis. FEBS letters, 2011. 585(23): p. 3675–3680. [PubMed: 21550343]
44. Ding Y, et al. , Progranulin promotes bone fracture healing via TNFR pathways in mice with type 2 diabetes mellitus. Annals of the New York Academy of Sciences, 2021. 1490(1): p. 77–89. [PubMed: 33543485]
45. Zhao Y. p., et al. , The promotion of bone healing by progranulin, a downstream molecule of BMP-2, through interacting with TNF/TNFR signaling. Biomaterials, 2013. 34(27): p. 6412–6421. [PubMed: 23746860]
46. Liu C. j. and Bosch X, Progranulin: a growth factor, a novel TNFR ligand and a drug target. Pharmacology & therapeutics, 2012. 133(1): p. 124–132. [PubMed: 22008260]
47. Katyal P, et al. , Injectable recombinant block polymer gel for sustained delivery of therapeutic protein in post traumatic osteoarthritis. Biomaterials, 2022. 281: p. 121370. [PubMed: 35032910]
48. Alizadeh A, et al. , Delivery of injectable thermo-sensitive hydrogel releasing nerve growth factor for spinal cord regeneration in rat animal model. Journal of Tissue Viability, 2020. 29(4): p. 359–366. [PubMed: 32839065]
49. Moradi L, et al. , Regeneration of meniscus tissue using adipose mesenchymal stem cells-chondrocytes co-culture on a hybrid scaffold: In vivo study. Biomaterials, 2017. 126: p. 18–30. [PubMed: 28242519]
50. Yin Y, et al. , The effects of a pulsed electromagnetic field on the proliferation and osteogenic differentiation of human adipose-derived stem cells. Medical science monitor: international medical journal of experimental and clinical research, 2018. 24: p. 3274. [PubMed: 29775452]
51. Williams JN, et al., The generation of closed femoral fractures in mice: a model to study bone healing. JoVE (Journal of Visualized Experiments), 2018(138): p. e58122.
52. Chanachai A, et al. , Pervaporation with chitosan/hydroxyethylcellulose (CS/HEC) blended membranes. Journal of Membrane Science, 2000. 166(2): p. 271–280.
53. Yang X, et al. , Well-dispersed chitosan/graphene oxide nanocomposites. ACS applied materials & interfaces, 2010. 2(6): p. 1707–1713. [PubMed: 20527778]

54. Behrouzian F, Razavi SM, and Alghooneh A, Evaluation of interactions of biopolymers using dynamic rheological measurements: Effect of temperature and blend ratios. Journal of Applied Polymer Science, 2017. 134(5).
55. Khosrozadeh A, et al. , Wettability and sound absorption of graphene oxide doped polymer hydrogel. Scientific Reports, 2021. 11(1): p. 1–11. [PubMed: 33414495]
56. Cheah WY, et al. , Antibacterial activity of quaternized chitosan modified nanofiber membrane. International journal of biological macromolecules, 2019. 126: p. 569–577. [PubMed: 30584947]
57. Şen F and Kahraman MV, Preparation and characterization of hybrid cationic hydroxyethyl cellulose/sodium alginate polyelectrolyte antimicrobial films. Polymers for Advanced Technologies, 2018. 29(7): p. 1895–1901.
58. Zhou HY, et al. , Glycerophosphate-based chitosan thermosensitive hydrogels and their biomedical applications. Carbohydrate polymers, 2015. 117: p. 524–536. [PubMed: 25498667]
59. Rahmanian-Devin P, Baradaran Rahimi V, and Askari VR, Thermosensitive chitosan-β-glycerophosphate hydrogels as targeted drug delivery systems: An overview on preparation and their applications. Advances in Pharmacological and Pharmaceutical Sciences, 2021. 2021.
60. Qin H, et al. , Preparation and characterization of chitosan/β-glycerophosphate thermal-sensitive hydrogel reinforced by graphene oxide. Frontiers in chemistry, 2018. 6: p. 565. [PubMed: 30555817]
61. Talaat W, et al. , Nanoscale thermosensitive hydrogel scaffolds promote the chondrogenic differentiation of dental pulp stem and progenitor cells: A minimally invasive approach for cartilage regeneration. International Journal of Nanomedicine, 2020: p. 7775–7789. [PubMed: 33116500]
62. Kim J, et al. , Graphene-incorporated chitosan substrata for adhesion and differentiation of human mesenchymal stem cells. Journal of Materials Chemistry B, 2013. 1(7): p. 933–938. [PubMed: 32262357]
63. Nazar V, et al. , Gelatin hydrogel reinforced by graphene oxide grafted chitosan for cartilage tissue engineering application. International Journal of Polymeric Materials and Polymeric Biomaterials, 2022: p. 1–12.
64. Tavakoli M, Karbasi S, and Soleymani Eil Bakhtiari S, Evaluation of physical, mechanical, and biodegradation of chitosan/graphene oxide composite as bone substitutes. Polymer-Plastics Technology and Materials, 2020. 59(4): p. 430–440.
65. Argüelles-Monal WM, et al. , Chitosan derivatives: Introducing new functionalities with a controlled molecular architecture for innovative materials. Polymers, 2018. 10(3): p. 342. [PubMed: 30966377]
66. Singh N, et al. , Chitosan-graphene oxide hydrogels with embedded magnetic iron oxide nanoparticles for dye removal. ACS Applied Nano Materials, 2019. 2(11): p. 7379–7392.
67. Wang Y, et al. , Chitosan degradation products promote nerve regeneration by stimulating schwann cell proliferation via miR-27a/FOXO1 axis. Molecular neurobiology, 2016. 53: p. 28–39. [PubMed: 25399953]
68. Hamilton V, et al. , Bone cell attachment and growth on well-characterized chitosan films. Polymer International, 2007. 56(5): p. 641–647.
69. Hoo SP, et al. , Preparation of a soft and interconnected macroporous hydroxypropyl cellulose methacrylate scaffold for adipose tissue engineering. Journal of Materials Chemistry B, 2013. 1(24): p. 3107–3117. [PubMed: 32261014]
70. Tohamy KM, et al. , Novel alginate/hydroxyethyl cellulose/hydroxyapatite composite scaffold for bone regeneration: In vitro cell viability and proliferation of human mesenchymal stem cells. International Journal of Biological Macromolecules, 2018. 112: p. 448–460. [PubMed: 29408578]
71. Gzyra-Jagieła K, et al. , Physicochemical properties of chitosan and its degradation products. Chitin and Chitosan: Properties and Applications, 2019: p. 61–80.
72. Ngoenkam J, et al. , Potential of an injectable chitosan/starch/β-glycerol phosphate hydrogel for sustaining normal chondrocyte function. International journal of pharmaceutics, 2010. 391(1–2): p. 115–124. [PubMed: 20206248]

73. Wu K, et al. , Fabrication of chitosan/graphene oxide composite aerogel microspheres with high bilirubin removal performance. Materials Science and Engineering: C, 2020. 106: p. 110162. [PubMed: 31753385]
74. Moradi S, et al. , Chitosan/graphene oxide composite films and their biomedical and drug delivery applications: A review. Applied Sciences, 2021. 11(17): p. 7776.
75. Wang K, et al. , Biocompatibility of graphene oxide, Nanoscale Res. Lett, 2010. 6(1): p. 8.
76. Lingaraju K, et al. , Biocompatible synthesis of reduced graphene oxide from Euphorbia heterophylla (L.) and their in-vitro cytotoxicity against human cancer cell lines. Biotechnology reports, 2019. 24: p. e00376. [PubMed: 31641620]
77. Cheng N-C, Wang S, and Young T-H, The influence of spheroid formation of human adipose-derived stem cells on chitosan films on stemness and differentiation capabilities. Biomaterials, 2012. 33(6): p. 1748–1758. [PubMed: 22153870]
78. Cheng NC, et al. , Efficient transfer of human adipose-derived stem cells by chitosan/gelatin blend films. Journal of Biomedical Materials Research Part B: Applied Biomaterials, 2012. 100(5): p. 1369–1377. [PubMed: 22566407]
79. Huang G-S, et al. , Spheroid formation of mesenchymal stem cells on chitosan and chitosan-hyaluronan membranes. Biomaterials, 2011. 32(29): p. 6929–6945. [PubMed: 21762982]
80. Cheng N-C, et al. , Engineered cartilage using primary chondrocytes cultured in a porous cartilage-derived matrix. Regenerative medicine, 2011. 6(1): p. 81–93. [PubMed: 21175289]
81. Lin I-C, et al. , Chitosan-cartilage extracellular matrix hybrid scaffold induces chondrogenic differentiation to adipose-derived stem cells. Regenerative Therapy, 2020. 14: p. 238–244. [PubMed: 32435677]
82. Vickers SM, Squitieri LS, and Spector M, Effects of cross-linking type II collagen-GAG scaffolds on chondrogenesis in vitro: dynamic pore reduction promotes cartilage formation. Tissue engineering, 2006. 12(5): p. 1345–1355. [PubMed: 16771647]
83. Du H, et al. , Cellulose nanocrystals and cellulose nanofibrils based hydrogels for biomedical applications. Carbohydrate polymers, 2019. 209: p. 130–144. [PubMed: 30732792]
84. Anju P, et al. , In situ synthesized hydro-lipophilic nano and micro fibrous bacterial cellulose: polystyrene composites for tissue scaffolds. Journal of Materials Science, 2020. 55(12): p. 5247–5256.
85. Nouri-Felekori M, et al. , Bioorthogonal hydroxyethyl cellulose-based scaffold crosslinked via click chemistry for cartilage tissue engineering applications. International Journal of Biological Macromolecules, 2021. 183: p. 2030–2043. [PubMed: 34097959]
86. Wu C, et al. , Graphene-oxide-modified β-tricalcium phosphate bioceramics stimulate in vitro and in vivo osteogenesis. Carbon, 2015. 93: p. 116–129.
87. Su J, et al. , Graphene oxide coated titanium surfaces with osteoimmunomodulatory role to enhance osteogenesis. Materials Science and Engineering: C, 2020. 113: p. 110983. [PubMed: 32487397]
88. Jang W, et al. , Direct-deposited graphene oxide on dental implants for antimicrobial activities and osteogenesis. International Journal of Nanomedicine, 2021. 16: p. 5745. [PubMed: 34471350]
89. Noh M, et al. , Graphene oxide reinforced hydrogels for osteogenic differentiation of human adipose-derived stem cells. RSC advances, 2017. 7(34): p. 20779–20788.
90. Li D and Kaner RB, Graphene-based materials. Science, 2008. 320(5880): p. 1170–1171. [PubMed: 18511678]
91. Hong J, et al. , Graphene multilayers as gates for multi-week sequential release of proteins from surfaces. Acs Nano, 2012. 6(1): p. 81–88. [PubMed: 22176729]
92. Murray E, et al. , Characterization of a human osteoblastic osteosarcoma cell line (SAOS-2) with high bone alkaline phosphatase activity. Journal of Bone and Mineral Research, 1987. 2(3): p. 231–238. [PubMed: 2843003]
93. Huang Z, et al. , Photoacoustic stimulation promotes the osteogenic differentiation of bone mesenchymal stem cells to enhance the repair of bone defect. Scientific Reports, 2017. 7(1): p. 15842. [PubMed: 29158525]
94. MacRae VE, et al. , Inhibition of PHOSPHO1 activity results in impaired skeletal mineralization during limb development of the chick. Bone, 2010. 46(4): p. 1146–1155. [PubMed: 20053388]

95. Sarkar J, et al. , Comparison of two mouse ameloblast-like cell lines for enamel-specific gene expression. Frontiers in physiology, 2014. 5: p. 277. [PubMed: 25120490]

96. Zhang E, et al. , Role of TNF-α in early-stage fracture healing under normal and diabetic conditions. Computer Methods and Programs in Biomedicine, 2022. 213: p. 106536. [PubMed: 34823199]

97. Jiao H, Xiao E, and Graves DT, Diabetes and its effect on bone and fracture healing. Current osteoporosis reports, 2015. 13(5): p. 327–335. [PubMed: 26254939]

98. Wagner JM, et al. , Inhibition of Pathological Increased Matrix Metalloproteinase (MMP) Activity for Improvement of Bone Regeneration in Diabetes. Life, 2022. 12(2): p. 134. [PubMed: 35207422]

99. Kayal RA, et al. , TNF-α mediates diabetes-enhanced chondrocyte apoptosis during fracture healing and stimulates chondrocyte apoptosis Through FOXO1. Journal of Bone and Mineral Research, 2010. 25(7): p. 1604–1615. [PubMed: 20200974]

100. Alquézar C, et al. , Progranulin deficiency induces overactivation of WNT5A expression via TNF-α/NF-κB pathway in peripheral cells from frontotemporal dementia-linked granulin mutation carriers. Journal of Psychiatry and Neuroscience, 2016. 41(4): p. 225–239. [PubMed: 26624524]

101. Wang BC, et al. , New discovery rarely runs smooth: an update on progranulin/TNFR interactions. Protein & cell, 2015. 6(11): p. 792–803. [PubMed: 26408020]

102. Wang S, et al. , Progranulin is positively associated with intervertebral disc degeneration by interaction with IL-10 and IL-17 through TNF pathways. Inflammation, 2018. 41(5): p. 1852–1863. [PubMed: 29992506]

103. Tang W, et al. , The growth factor progranulin binds to TNF receptors and is therapeutic against inflammatory arthritis in mice. Science, 2011. 332(6028): p. 478–484. [PubMed: 21393509]

104. Murugaiyan K, et al. , Role of FGF-18 in Bone Regeneration. Journal of Functional Biomaterials, 2023. 14(1): p. 36. [PubMed: 36662083]

105. Nagayama T, et al. , FGF18 accelerates osteoblast differentiation by upregulating B mp2 expression. Congenital anomalies, 2013. 53(2): p. 83–88. [PubMed: 23751042]

106. Capasso TL, et al. , BMP10-mediated ALK1 signaling is continuously required for vascular development and maintenance. Angiogenesis, 2020. 23: p. 203–220. [PubMed: 31828546]

107. David L, et al. , Identification of BMP9 and BMP10 as functional activators of the orphan activin receptor-like kinase 1 (ALK1) in endothelial cells. Blood, 2007. 109(5): p. 1953–1961. [PubMed: 17068149]

108. Fujioka-Kobayashi M, et al. , Cholesteryl group-and acryloyl group-bearing pullulan nanogel to deliver BMP2 and FGF18 for bone tissue engineering. Biomaterials, 2012. 33(30): p. 7613–7620. [PubMed: 22800537]

109. He X, et al. , BMP2 genetically engineered MSCs and EPCs promote vascularized bone regeneration in rat critical-sized calvarial bone defects. PloS one, 2013. 8(4): p. e60473. [PubMed: 23565253]

110. Zhao Q, et al. , Parallel expression of Sox9 and Col2a1 in cells undergoing chondrogenesis. Developmental dynamics: an official publication of the American Association of Anatomists, 1997. 209(4): p. 377–386. [PubMed: 9264261]

111. Rico-Llanos GA, et al. , Collagen type I biomaterials as scaffolds for bone tissue engineering. Polymers, 2021. 13(4): p. 599. [PubMed: 33671329]

112. Hankenson K, Gagne K, and Shaughnessy M, Extracellular signaling molecules to promote fracture healing and bone regeneration. Advanced drug delivery reviews, 2015. 94: p. 3–12. [PubMed: 26428617]

113. Majidinia M, Sadeghpour A, and Yousefi B, The roles of signaling pathways in bone repair and regeneration. Journal of cellular physiology, 2018. 233(4): p. 2937–2948. [PubMed: 28590066]

114. Huh J-E, et al. , Mangiferin reduces the inhibition of chondrogenic differentiation by IL-1β in mesenchymal stem cells from subchondral bone and targets multiple aspects of the Smad and SOX9 pathways. International Journal of Molecular Sciences, 2014. 15(9): p. 16025–16042. [PubMed: 25216336]

115. Mao C, et al. , Double-edged-sword effect of IL-1β on the osteogenesis of periodontal ligament stem cells via crosstalk between the NF-κB, MAPK and BMP/Smad signaling pathways. Cell death & disease, 2016. 7(7): p. e2296–e2296. [PubMed: 27415426]

116. Takeuchi T, Yoshida H, and Tanaka S, Role of interleukin-6 in bone destruction and bone repair in rheumatoid arthritis. Autoimmunity Reviews, 2021. 20(9): p. 102884. [PubMed: 34229044]

117. Nemoto E, et al. , Wnt5a signaling is a substantial constituent in bone morphogenetic protein-2-mediated osteoblastogenesis. Biochemical and biophysical research communications, 2012. 422(4): p. 627–632. [PubMed: 22609204]

118. Zhang W, et al. , Overexpression of HSPA1A enhances the osteogenic differentiation of bone marrow mesenchymal stem cells via activation of the Wnt/β-catenin signaling pathway. Scientific reports, 2016. 6(1): p. 27622. [PubMed: 27279016]

119. Houschyar KS, et al. , Wnt pathway in bone repair and regeneration–what do we know so far. Frontiers in cell and developmental biology, 2019. 6: p. 170. [PubMed: 30666305]

120. Kamiya N, et al., BMP signaling negatively regulates bone mass through sclerostin by inhibiting the canonical Wnt pathway. 2008.

121. Maeda K, et al. , Wnt5a-Ror2 signaling between osteoblast-lineage cells and osteoclast precursors enhances osteoclastogenesis. Nature medicine, 2012. 18(3): p. 405–412.

122. Baron R and Kneissel M, WNT signaling in bone homeostasis and disease: from human mutations to treatments. Nature medicine, 2013. 19(2): p. 179–192.

123. Kong L, et al. , Extracellular matrix protein 1, a direct targeting molecule of parathyroid hormone–related peptide, negatively regulates chondrogenesis and endochondral ossification via associating with progranulin growth factor. The FASEB Journal, 2016. 30(8): p. 2741. [PubMed: 27075243]

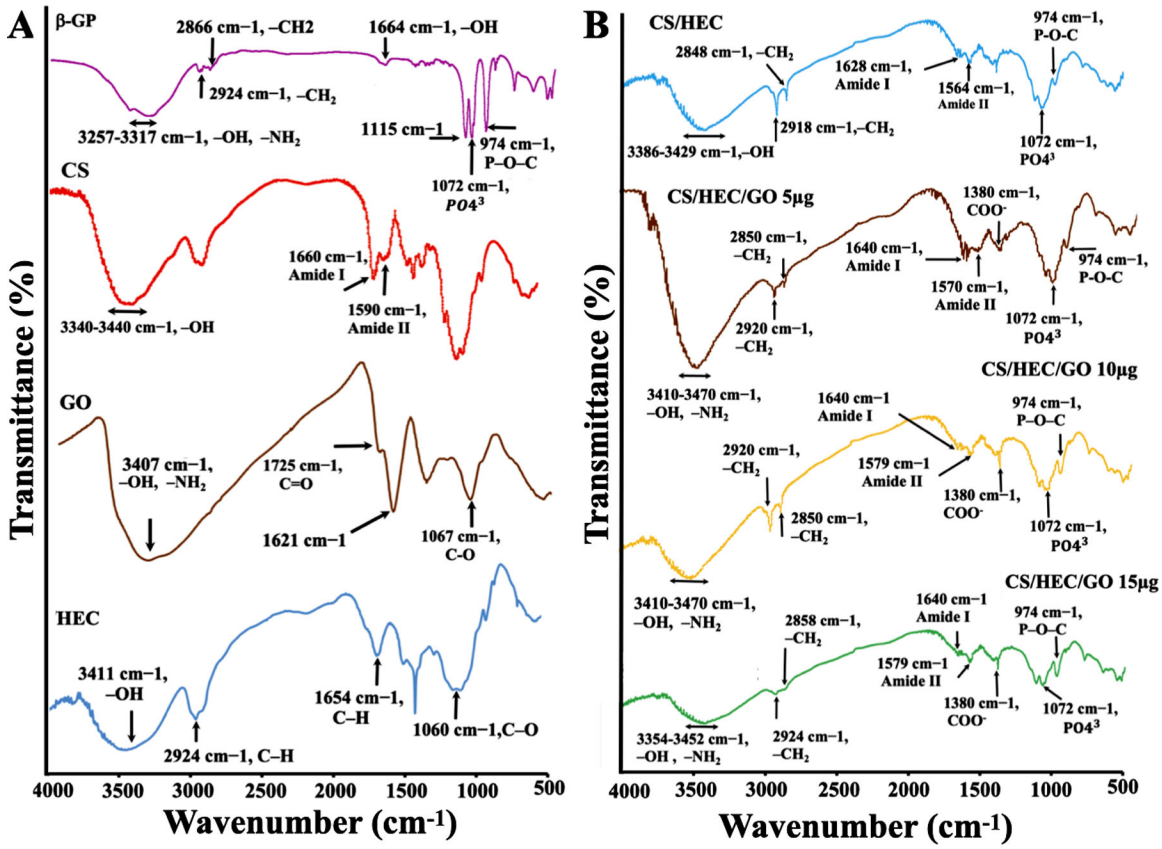

Fig. 1. FTIR spectra.

FTIR spectra of **A)** pure β-GP, CS, GO, and HEC. **B)** CS/HEC, CS/HEC/GO 5µg, CS/HEC/GO 10 µg, and CS/HEC/GO 15 µg hydrogels formulations were examined. Each spectrum revealed characteristic peaks corresponding to the functional groups present in the respective compounds. The analysis of these individual spectra allowed for the identification and characterization of the specific molecular components.

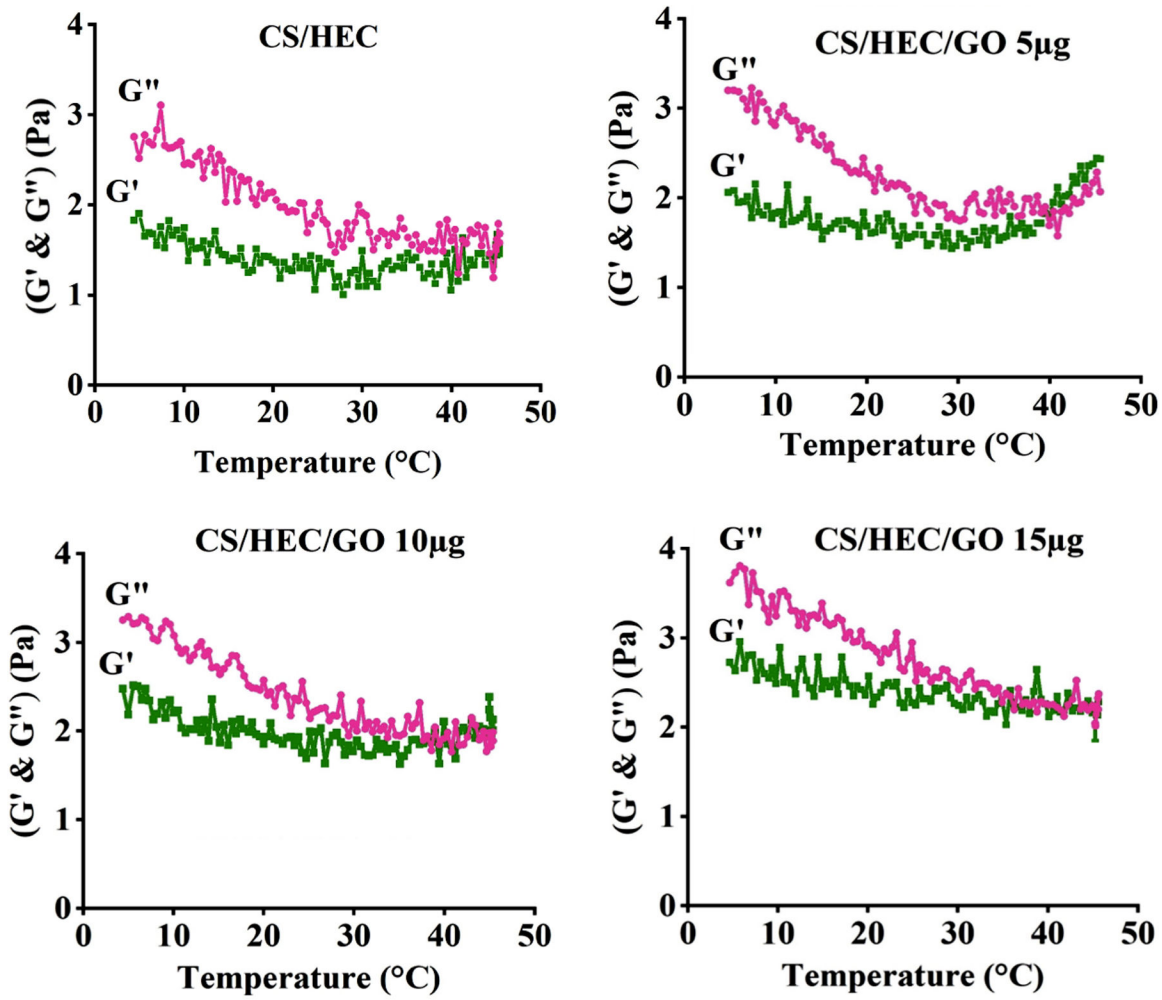

Fig. 2. Rheology properties of the hydrogels across a temperature range spanning from 4 to 45 °C.

The experimental data allowed for the construction of curves representing the storage and loss moduli (G′ & G″) as a function of temperature (°C) for the different hydrogel formulations, namely CS/HEC, CS/HEC/GO 5 µg, CS/HEC/GO 10 µg, and CS/HEC/GO 15 µg hydrogels.

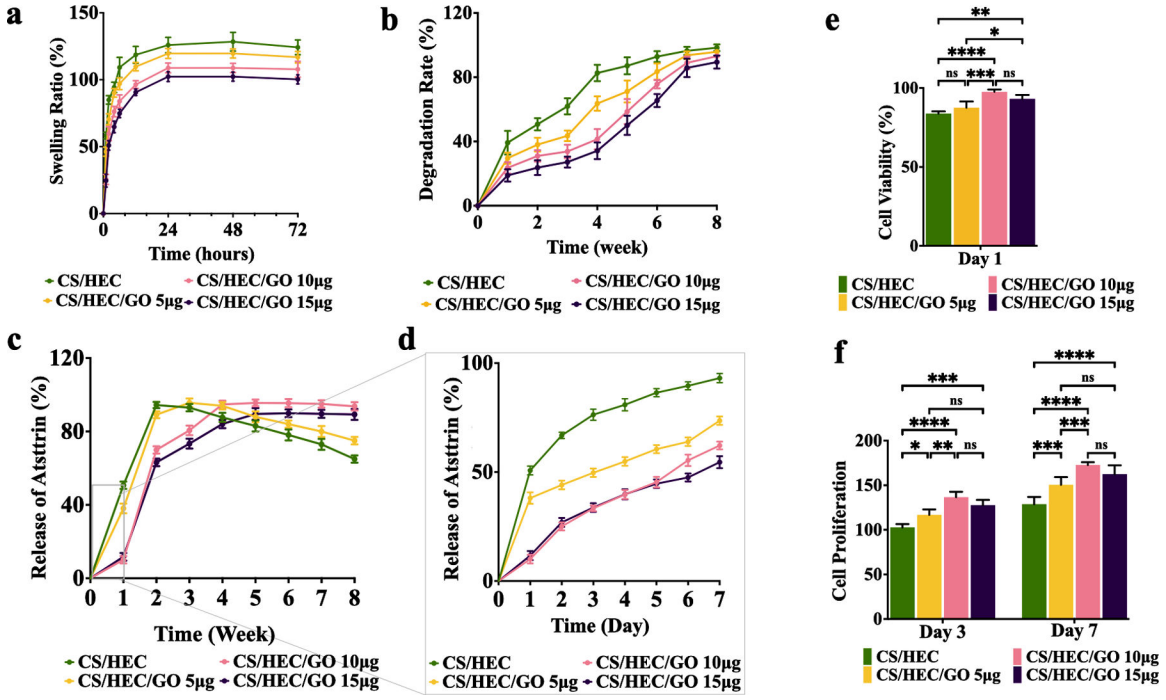

Fig. 3. In vitro characterization of hydrogels.

a) The swelling rate of the prepared CS/HEC, CS/HEC/GO 5 µg, CS/HEC/GO 10 µg, and CS/HEC/GO 15 µg hydrogels in PBS within 72 hours. **b)** The degradation rate of the prepared CS/HEC, CS/HEC/GO 5 µg, CS/HEC/GO 10 µg, and CS/HEC/GO 15 µg hydrogels in PBS within 8 weeks. **c)** The release curves represent Atsttrin release into PBS at 37 °C over 8 weeks from CS/HEC, CS/HEC/GO 5 µg, CS/HEC/GO 10 µg and CS/HEC/GO 15 µg hydrogels. **d)** Represents the data for the first 7 days or the first week. The experiments were done in 3 replicates. **e)** The cytocompatibility evaluation of the hydrogels in contact with bmMSCs by MTT assay at 24 hours post-incubation. **f)** Cell proliferation assay at day 3 and 7 after incubation. Two-way ANOVA shows significant differences between the experimental and control group (*$p < 0.05$; **$p < 0.01$; ***$p < 0.001$; ****$p < 0.0001$). The experiments were done in 5 biological replicates (n=5), and the data presented are mean ± SD.

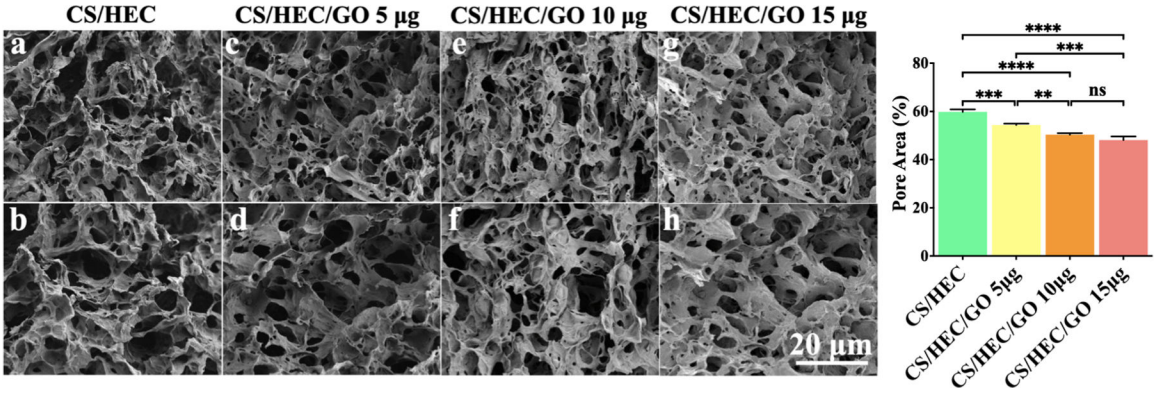

Figure. 4.

SEM imaging of prepared hydrogels. Cross-sectional SEM images of the prepared hydrogels (a–h). Effect of GO amount on the percentage of pore area (i) of the hydrogels. One-way ANOVA determined the hydrogel with a higher concentration of GO showed a lower pore area, smaller pore size, and thicker pore wall. All the experiments were done in triplicate (n=3), and the data presented are mean ± SD, (** $P < 0.01$, ***$P < 0.001$, and, ****$P < 0.0001$).

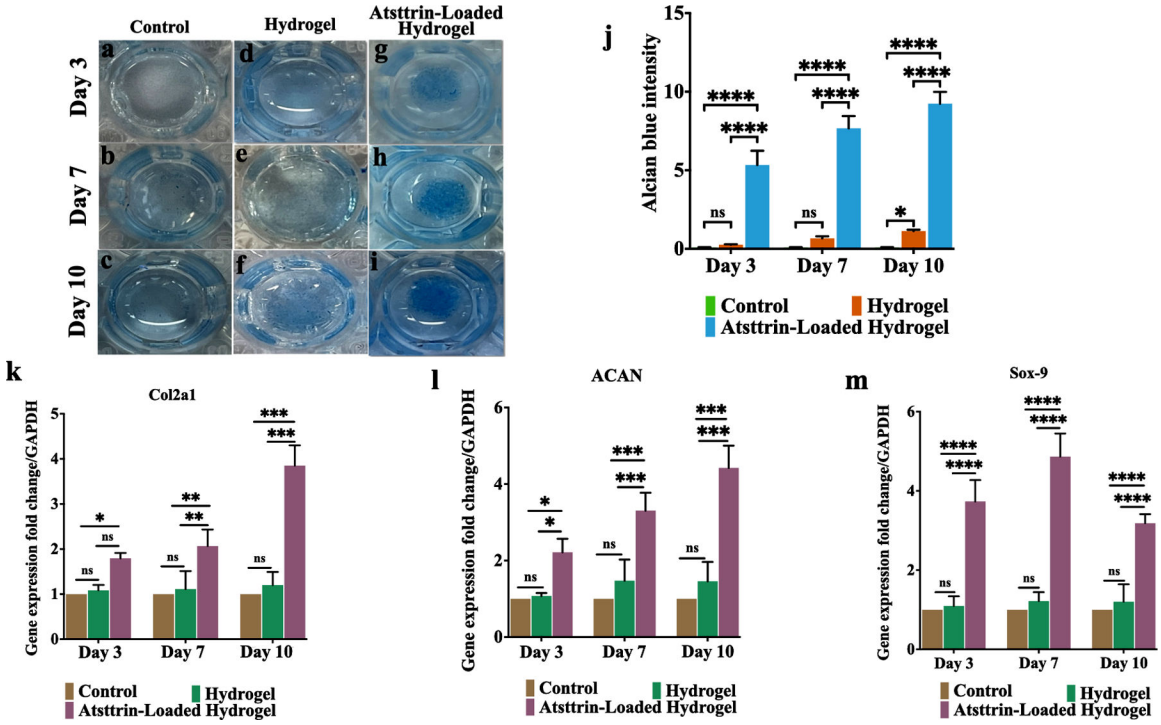

Fig. 5. Hydrogel loaded with Atsttrin promotes *in vitro* chondrogenesis.

Alcian blue staining (**a-i)** for bmMSCs treated with chondrogenic media (containing dexamethasone, ITS and, ascorbic acid) (control group) **(a, b, c)**, chondrogenic media + hydrogel alone (hydrogel group) **(d, e, f)**, and chondrogenic media + hydrogel loaded with 1000 ng/mL Atsttrin (Atsttrin-loaded hydrogel group) **(g, h, i)** for 10 days. Quantitative analysis of GAGs deposition of bmMSCs during 10 days of incubation **(j)**. Real-time PCR analysis of Col2al **(k)**, ACAN **(l)**, and Sox-9 **(m)** at days 3, 7, and 10. Normalized values were calibrated against controls and set as 1. Experiments were conducted in triplicate (n=3). Values are presented as mean ± SD of three independent experiments. The asterisk indicates statistically significant differences between the control and experience groups (∗p < 0.05; ∗∗p < 0.01; ∗∗∗p < 0.001; ∗∗∗∗p < 0.0001).

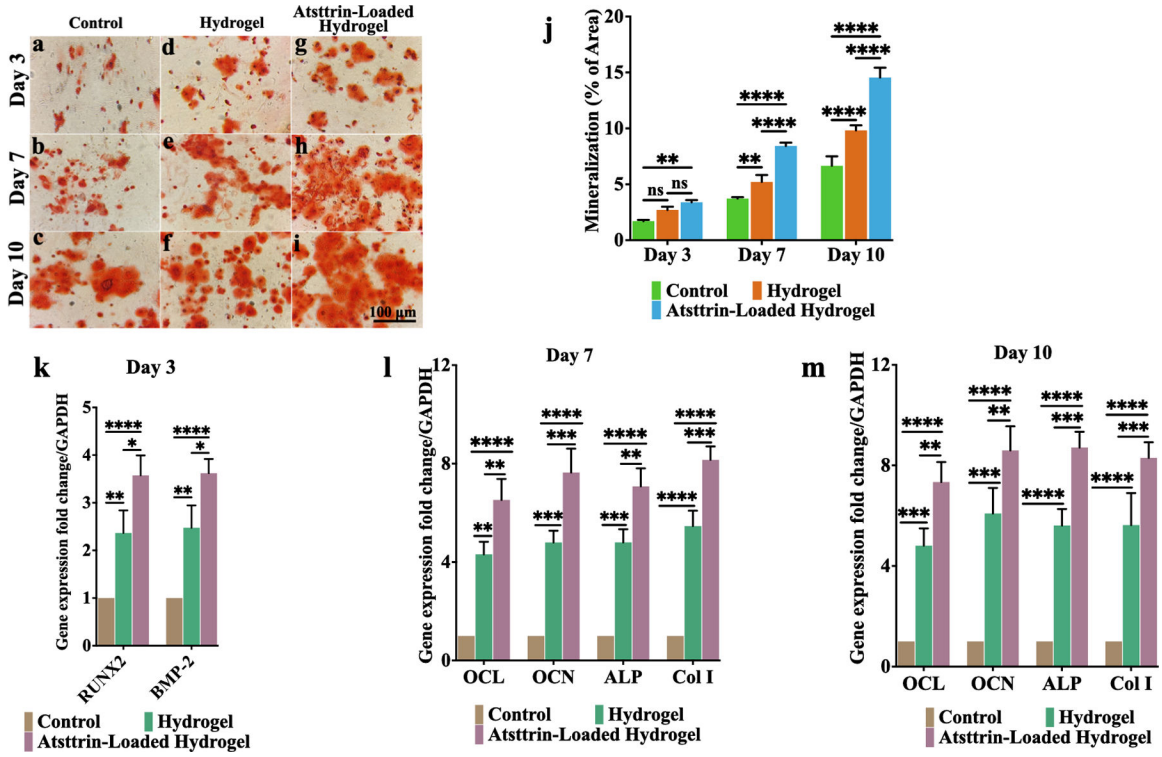

Fig. 6. Effect of Atsttrin released from hydrogel on osteogenic differentiation of bmMSCs.

Alizarin red staining of bmMSCs treated with osteogenic culture medium alone (control group) **(a, b, c)**, hydrogel alone + osteogenic culture medium **(d, e, f)**, and hydrogel-loaded with 1000 ng/mL Atsttrin + osteogenic culture medium **(g, h, i)** for 10 days. Quantitative analysis of mineral deposition of bmMSCs during 10 days of incubation **(j)**. Real-time PCR analysis **(k, l, m)** of RUNX-2, BMP-2, OCL, OCN, ALP, and Col I expression of bmMSCs after treated with osteogenic media, hydrogel + osteogenic culture media and Atsttrin-loaded hydrogel + osteogenic media for 3, 7 and 10 days. The asterisk indicates statistically significant differences between the control and experience groups (∗p < 0.05; ∗∗p < 0.01; ∗∗∗p < 0.001; ∗∗∗∗p < 0.0001). The scale bar represents 100 μm. Values are presented as mean ± SD of three independent experiments. Experiments were conducted in triplicate (n=3)

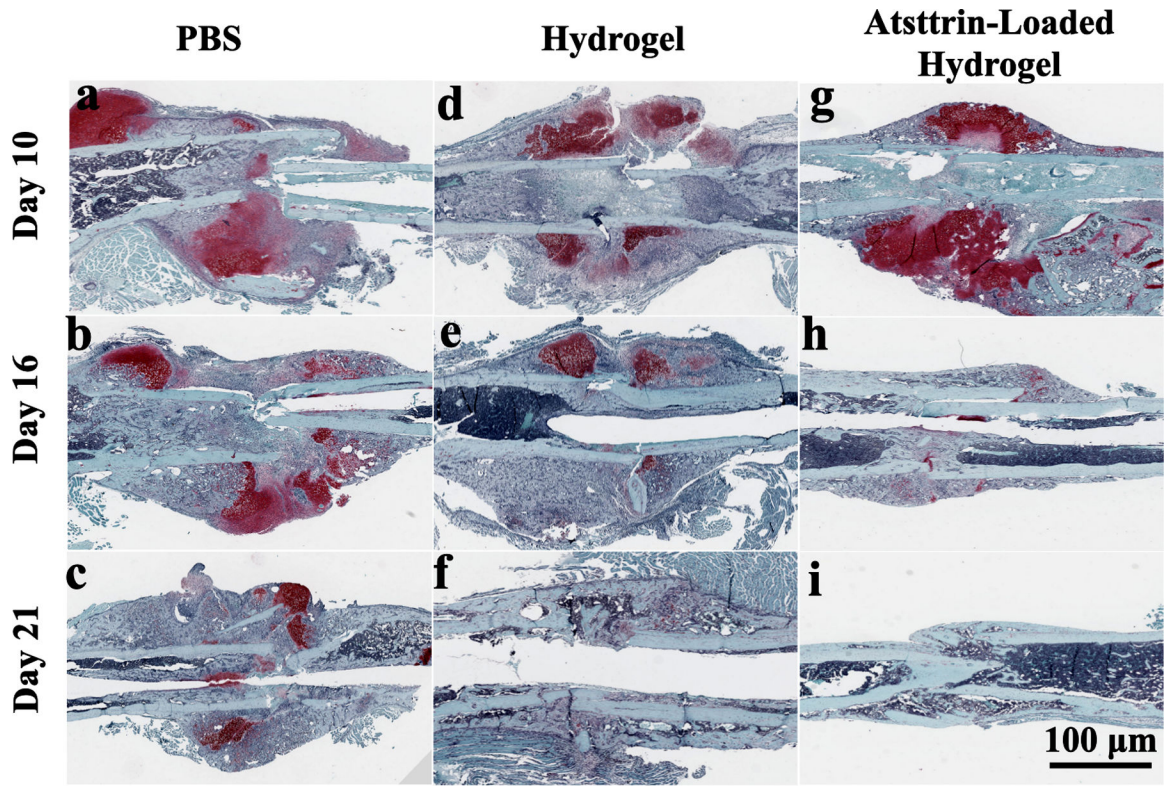

Fig. 7. Atsttrin-loaded hydrogel promotes T1DM-delayed bone healing in closed gravity bone fracture mouse model.

Longitudinal sections of the fracture callus area at postoperative days 10, 16, and 21 are shown by Safranin O/Fast green staining images for PBS (control) (a, b, c), hydrogel (d, e, f) and Atsttrin-loaded hydrogel (g, h, i) groups. Cartilaginous matrix is specifically marked in a reddish color while mineralized tissue is observed as blue. Endochondral ossification was promoted in the group treated with Atsttrin-loaded hydrogel followed by the hydrogel group compared with the control group. The scale bar represents 100 μm. Six femur samples were used for the histology evaluation.

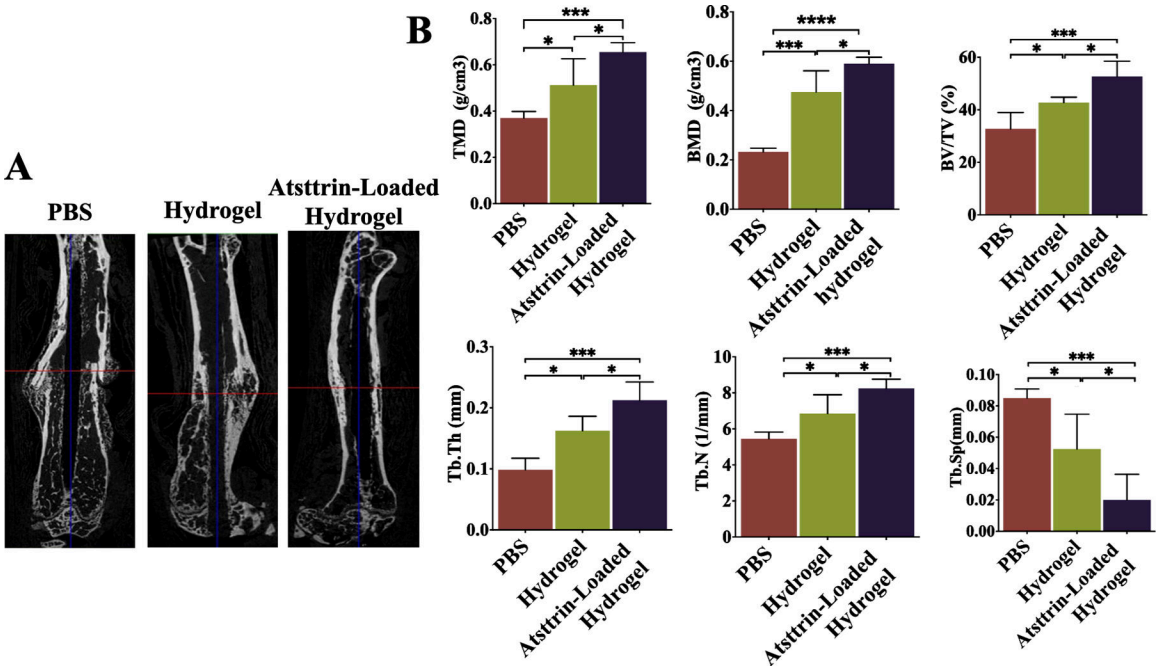

Fig. 8. Micro-computed tomography (MicroCT) analysis.

MicroCT analysis indicates that Atsttrin-loaded hydrogel promoted callus formation and the subsequent bone remodeling process during fracture healing in diabetic mice. **A)** Representative microCT longitudinal section images of femurs reveal the state of healing of the bone fractures after 3 weeks in PBS, hydrogel, and Atsttrin-loaded hydrogel groups. The images were used to qualitatively assess callus size and healing state. **B)** Quantitative evaluation of fracture callus in diabetic mice by the analyzing parameter of microCT including tissue mineral density (TMD; g/cm^3), bone mineral density (BMD; g/cm^3), bone volume fraction (BV/TV, %), trabecular thickness (Tb. Th; mm), trabecular number (Tb. N; 1/mm), and trabecular spacing (Tb.S; mm) at day 21 after inducing closed gravity femur fracture followed by treatment with PBS (n = 3), hydrogel (n = 3), and Atsttrin-loaded hydrogel (n = 3). Values are presented as mean ± SD. Significance was determined via One-Way ANOVA followed by Dunnet's test for multiple comparisons. *p < 0.05, **p < 0.01, *** p <0.001; **** p <0.0001.

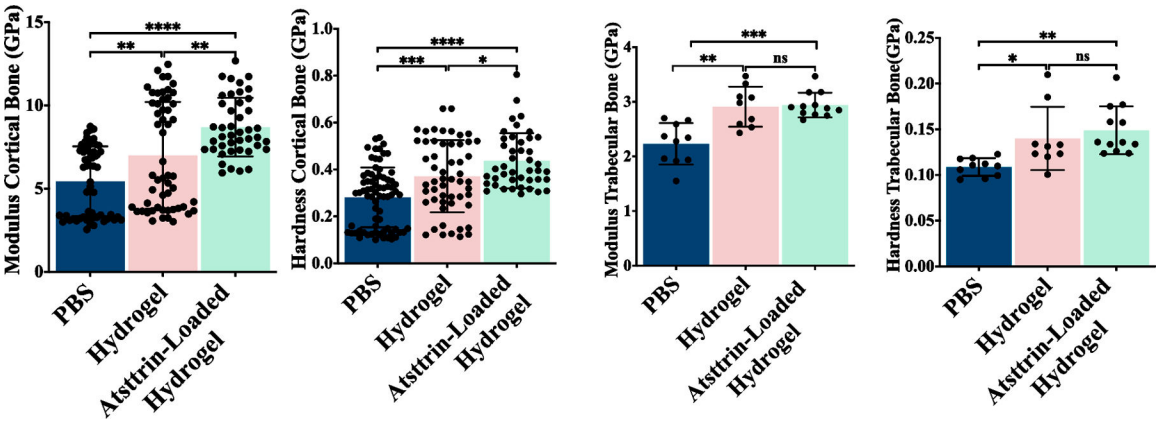

Fig. 9. Nanoindentation test.

A) Nanoindentation tests assess the mechanical properties of the fracture site at 21 days post-fracture in PBS (n = 3), hydrogel (n = 3), and Atsttrin-loaded hydrogel (n = 3) groups. Modulus (GPa) and hardness (GPa) for both cortical and trabecular bone of the fracture site were measured. Values presents are as mean ± SD. Significance was determined via One-Way ANOVA followed by Dunnet's test for multiple comparisons. *p < 0.05, **p < 0.01, *** p <0.001, **** p <0.0001.

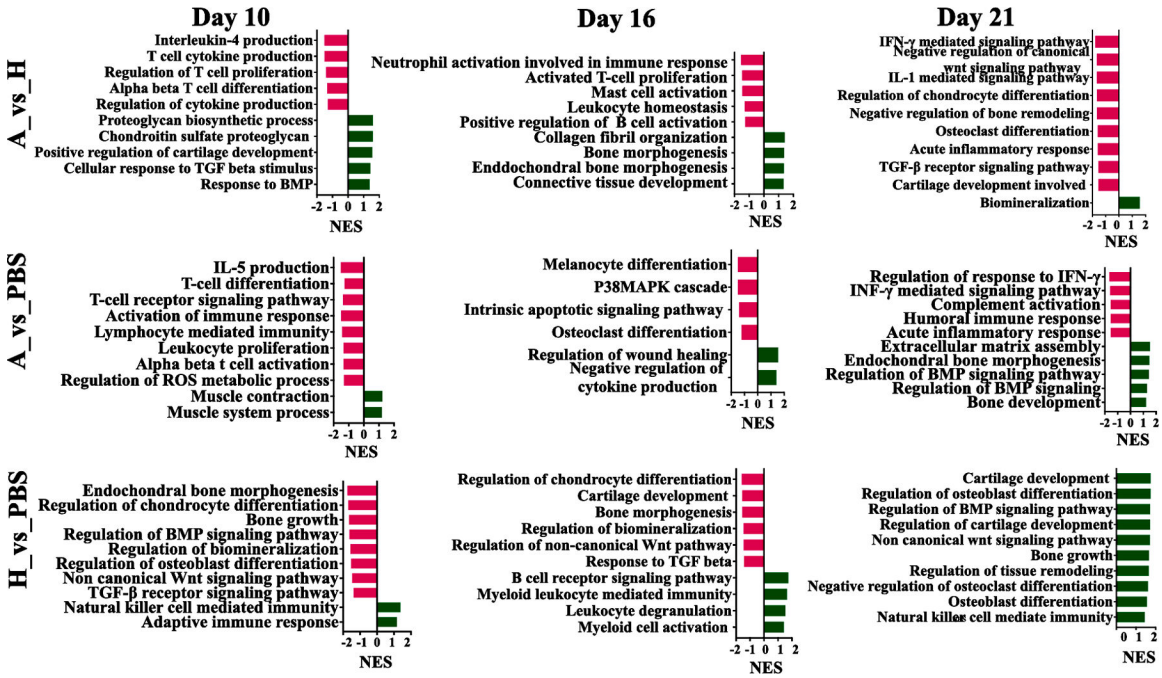

Figure .10. GSEA Analysis.

GSEA plots with gene ontology biological process gene sets are shown for the Atsttrin-loaded hydrogel, hydrogel and PBS-treated groups during healing and at day 10, 16, and 21 post-fracture. Red and green bars represent the down-regulated and up-regulated signal pathways, respectively. Atsttrin-loaded hydrogel_vs_Hydrogel (A_vs_H), Atsttrin-loaded hydrogel_vs_PBS (A_vs_PBS), and Hydrogel_vs_PBS (H_vs_PBS). The Normalized Enrichment Scores (NES) are indicated.